DOCK5 couples CDC42-GSK3β activation with focal adhesion morphogenesis to reinforce the establishment of polarity and promote YAP/TAZ activation during migration.

Patricia Pascual-Vargas[1], Mar Arias-Garcia[1], Theodoros I. Roumeliotis[1], Jyoti S.Choudhary[1], and Chris Bakal[1].

[1] Chester Beatty Laboratories, Division of Cancer Biology, Institute of Cancer Research, 237 Fulham Road, London SW3 6JB, UK

Corresponding authors: patricia.pascualvargas@icr.ac.uk and Chris Bakal chris.bakal@icr.ac.uk

ORCID:
Patricia Pascual-Vargas: https://orcid.org/0000-0001-5246-6361
Chris Bakal: https://orcid.org/0000-0002-0413-6744

Abstract

YAP and TAZ are transcriptional co-activators that are often constitutively active in triple negative breast cancer (TNBC) cells. However the mechanisms responsible for YAP/TAZ dysregulation in TNBC remain unclear. We hypothesised that RhoGEF activity in TNBC cells underpins YAP/TAZ activation in TNBC cells. Through systematic RNAi screening we found that the Focal Adhesion (FA) associated RhoGEF DOCK5 promotes YAP/TAZ nuclear translocation in proliferating TNBC cells. DOCK5 is required for 2D migration and 3D invasion, acting as a coincident detector that maintains cell polarity by stabilising GSK3β activation downstream of CDC42 at polarised leading edges only where FAs are being assembled. DOCK5 and CDC42 are required for cell survival and drug resistance in TNBC cells. Based on these studies we propose that cancer cell phenotypes such as drug resistance can be driven by cells adopting polarised, migratory shapes.

Introduction

Many cells migrate in polarised ways by establishing a single polarised front, or leading edge. The polarised front is the site of dynamic actin reorganisation that generates protrusive structures and rapid actomyosin retrograde flow, and is the primary point of attachment to the extra-cellular matrix (ECM) by integrin-rich focal adhesions (FAs)[1,2]. Critically, despite constant turnover of both actin and integrin-based structures at the leading edge, many cells are able to maintain polarity for long periods of time and migrate in highly processive manners. However, how such polarity is maintained is unclear.

The activity of Rho-family GTPases is critically important to migration and to the formation of leading-edge structures. For example, CDC42 activation establishes polarity and promotes the formation of protrusive filopodia[3,4]. The activation of RAC-type (RAC1, RAC2) GTPases promotes FA growth, and reorganises actin at the leading edge[5,6]. Signalling by RHOA GTPase promotes actomyosin tension which is key for the generation of traction at FAs[7–9]. But how the activity of these Rho GTPases is coordinated in migrating cells over dynamically changing cell space, and over time scales that range from milliseconds to hours, is very poorly understood. The ability of some cancer cells to aggressively metastasise suggests that they have evolved mechanisms to coordinate Rho GTPase activity in ways that favour persistent migration and invasion[10–14].

Rho GTP Exchange Factors (RhoGEFs) activate Rho GTPases by catalysing the exchange of GDP for GTP, while Rho GTP-Activating Proteins (RhoGAPs) induce GTP hydrolysis and inactivate Rho GTPases[15,16]. RhoGEFs and RhoGAPs have a number of protein-protein and protein-lipid interaction domains that mediate their recruitment to specific subcellular structures such as the membrane, nucleus, or focal adhesions[17]. At these specific milieus, RhoGEFs/RhoGAPs tightly regulate the spatiotemporal regulation of Rho GTPases, and even dictate the effectors that are recruited by Rho GTPases themselves[16,18]. RhoGEFs/RhoGAPs can also act as non-enzymatic scaffolds that can act to assemble large signalling complexes that can act independently

of, or in concert with, Rho GTPase activity[19]. Because of their ability to tightly regulate Rho GTPase and other signalling pathways in time and space, RhoGEFs and RhoGAPs are essential regulators of cell morphogenesis, migration and invasion in all eukaryotic cells[11,15,19,20].

Significant upregulation of RhoGEF mRNA and/or protein levels has been observed in breast cancer tissue[14,21–26]. Further, the RhoGEFs *OBSCN* and *FGD5* have been found to be mutated in breast cancers[19,22,23,27,28]. While the dysregulated activity of RhoGEFs has been implicated in driving the metastasis of cancer cells, and in particular breast cancer cells[27,29–31] how RhoGEFs promote rapid changes in cytoskeleton, adhesion, and cell shape that drive processes essential to metastasis is largely unknown.

One target of increased RhoGEF and Rho GTPase activity in all mammalian cells are the YAP and TAZ (hereafter referred to as YAP/TAZ) transcriptional coactivators. YAP/TAZ can promote a number of cancer relevant behaviours such as increased survival, proliferation, drug resistance, the Epithelial-to-Mesenchymal Transition (EMT), migration, and invasion[32–35]. In normal cells, sequestration of YAP/TAZ proteins to the cytoplasm renders them inactive, and nuclear translocation of YAP/TAZ is trigged by soluble, mechanical, and geometrical cues[33,35–43]. Activation of YAP/TAZ is frequently observed in many cancer subtypes, and especially in breast cancer cells, although YAP/TAZ themselves are very rarely mutated in breast cancers[44,45]. Moreover, the evolved drug resistance of many cancers is due to dysregulation of YAP/TAZ activity[46–53]. However, the mechanisms that lead to increased YAP/TAZ activity in cancers, and TNBCs are very poorly understood.

Increased activation of Rho GTPases can promote YAP/TAZ nuclear translocation in cancer cells through both direct and indirect means. Specifically, Rho GTPases alter the actin cytoskeleton resulting in YAP/TAZ activation in ways which are still largely unclear[33–35]. Alternatively, Rho GTPases can recruit and activate enzymes such as PAK2 and ROCK, which likely promote YAP/TAZ translocation directly[42]. Dysregulation of RhoGEF activity can potentially explain YAP/TAZ activation in many cancer cells, and

indeed oncogenic RhoGEFs such as TRIO have been found to promote YAP/TAZ nuclear translocation and activation[54,55]. Finally, in cases where YAP/TAZ upregulation leads to evolved drug resistance, increased YAP/TAZ activation is almost always linked to changes in cell shape, suggesting that changes in RhoGEF-Rho signaling are important drivers of this resistance[47,49,53,56–59].

We sought to understand the basis for increased YAP/TAZ activity in LM2 metastatic cells by performing high-throughput screening where we simultaneously measured YAP/TAZ nuclear translocation and cell shape following systematic knockdown of the majority of human RhoGEFs and RhoGAPs. These screens led to the identification of DOCK5 as an essential regulator of YAP/TAZ activity in metastatic cells. We show that DOCK5 acts as a coincident detector that sustains CDC42-GSK3β signalling, and thus maintains polarity, in subcellular regions that are also making stable attachments to the FAs. By maintaining polarity only in FA rich regions, DOCK5 promotes adoption of polarised cell shapes that are capable of processive migration, and that maintain YAP/TAZ activation. Thus DOCK5 regulates cell fates by promoting adoption of a polarised migratory form, which upregulates YAP/TAZ activity that can ultimately drive disease. Indeed, DOCK5 is essential for cell migration on 2D and their invasion of 3D collagen matrices, TNBC survival, and drug resistance. Our findings imply that cell behaviours underpinning oncogenesis and metastasis can in part be driven by cells adopting first a polarised shape capable of processive migration, and that such migration may not necessarily be a consequence of cancer driving events.

Results

DOCK5 depletion lowers YAP/TAZ nuclear translocation

LM2 cells are a metastatic derivative of MDA-MB-231 TNBC cells[31]. We have previously observed that in sub-confluent LM2 cells, YAP/TAZ proteins are predominantly nuclear[60]. In fact, compared to the TNBC cell lines hs578t and

SUM159, and the nonmetastatic mammary carcinoma cell line T47D, LM2 cells display much higher nuclear YAP/TAZ at subconfluent densities (Supplemental Figure 1A)**.** Increasing cell density of LM2 cell populations to high levels (2.0 x 10^5 cells per ml) does reduce YAP/TAZ nuclear translocation in LM2 cells, demonstrating that YAP/TAZ in LM2 remains partially sensitive to cell numbers as in normal tissues[42,61] (Supplemental Figure 1a). High basal levels of nuclear YAP/TAZ in sub-confluent LM2 cells also contrasts to those observed in MCF10A normal breast epithelial cells (Supplementary Figure 1a)[42]. Throughout this study we used LM2 cells at low density (3.3 x 10^4 cells per ml).

To identify regulators of Rho GTPases that contribute to the regulation of YAP/TAZ dynamics in TNBC cells, we systematically depleted 82 RhoGEFs, 67 GAPs and 19 Rho GTPases in LM2 cells and quantified the ratio of nuclear to cytoplasmic YAP/TAZ as a proxy for YAP/TAZ activation[33,42]. *LATS1, YAP* and *ECT2* siRNAs were used as positive controls[60]: si*LATS1/2* for our ability to assess YAP/TAZ localisation, as YAP/TAZ nuclear localisation is expected to increase in the absence of LATS1/2 [62]; si*YAP* for our ability to detect YAP/TAZ protein; and si*ECT2* to assess transfection efficiency as *ECT2* depletion results in multinucleate cells[63,64].

Knocking down individual Rho-family GTPases had distinct effects on YAP/TAZ nuclear translocation Specifically, knockdown of CDC42, and RHOA resulted in a significant drop in nuclear YAP/TAZ (Fig. 1a). Knockdown of either RAC1 or RAC3 led to statistically insignificant decreases in nuclear YAP/TAZ, while knockdown of RAC2 led to a moderate decrease (Fig. 1a). Thus the basal levels of YAP/TAZ activation observed in LM2 TNBC cells are partially due to the activation of CDC42 and RHOA.

To identify RhoGEFs that might be responsible for basal activation of YAP/TAZ in LM2 cells, we focused on RhoGEF siRNAs that reproducibly decrease nuclear YAP/TAZ levels. *DOCK5* siRNA was amongst the most consistent hits for low YAP/TAZ ratio (Fig. 1b), suggesting it is required for basal levels of

YAP/TAZ activation in LM2 cells. 4 out of 4 replicates of *DOCK5* siRNA were considered hits in our initial screen (Supplementary Table 1). We performed the same screen using another siRNA library (Dharmacon siGENOME; siG), which resulted in DOCK5 also being a hit for 4 out of 4 replicates (Supplementary Figure 1b). Using both the OTP and siGENOME siRNA depleting DOCK5 consistently reduced YAP/TAZ ratio without changing the total levels of YAP/TAZ levels (Fig. 1c, Supplementary Figure 1d), suggesting that DOCK5 is regulating YAP/TAZ nuclear translocation dynamics.

To validate that decreases in YAP/TAZ ratio were due to DOCK5 depletion, we quantified mRNA expression levels following OTP and siGENOME knockdown of *DOCK5* by quantitative RT-PCR and found that *DOCK5* mRNA expression levels were significantly reduced (Fig. 1d, Supplementary Figure 1c). We also tested the ability of each individual sequence from the two different siRNA pools (OTP and siG) to knockdown *DOCK5* mRNA and found that they all did so effectively (Supplementary Figure 1c). Further, all siRNAs except for OTP6 significantly reduced YAP/TAZ ratio, and none but siG3 reduced total YAP/TAZ levels (Supplementary Figure 1d). Because it is virtually impossible that different DOCK5 siRNAs would knockdown DOCK5 protein and have similar off-target effects, these data suggest that the decrease in YAP/TAZ ratio observed as a result of *DOCK5* siRNA is due to the specific on-target depletion of DOCK5 protein.

To corroborate our immunofluorescence imaging-based observations that DOCK5 depletion affects YAP/TAZ nuclear translocation, we performed subcellular fractionation of mock and DOCK5 depleted LM2 cells. In DOCK5 depleted cells the cytoplasmic fraction had significantly higher levels of both YAP and TAZ, compared to the same fraction from mock transfected cells. The ratios of nuclear to cytoplasmic YAP, TAZ, and YAP/TAZ were also significantly lower (Fig. 1e). The total amount of DOCK5 protein present in all fractions for mock and si*DOCK5* transfected cells showed that DOCK5 protein was significantly reduced with si*DOCK5* (Supplementary Figure 1e), indicating that *DOCK5* siRNA is indeed specifically depleting DOCK5 as expected.

To test the role of DOCK5 GEF activity on YAP/TAZ translocation we used C21, an inhibitor which blocks DOCK5's DHR2 catalytic domain, specifically hindering the interaction between DOCK5 and RAC1[65]. Treatment with C21 decreased YAP/TAZ by the same amount as *DOCK5* siRNA (Fig. 1f). These results obtained using a different reagent that inhibits DOCK5 activity both validate our finding that depletion of DOCK5 by siRNA reduces nuclear YAP/TAZ and demonstrate that DOCK5 catalytic activity is an essential component of how DOCK5 promotes YAP/TAZ nuclear translocation.

DOCK5 contributes to growth and drug resistance in LM2 cells

In many cell types, YAP/TAZ activation is essential for survival and/or proliferation[53,62,66–71]. To determine if DOCK5, Rho GTPases, and basal YAP/TAZ activity contribute to the survival of LM2 TNBC cells we performed growth curve assays over 160 hours to elucidate whether knockdown of these proteins affects growth. We normalised confluency values per condition to that of mock transfected cells per well, and compared fold change to mock at 50% confluency (Methods). DOCK5 depleted cells grew at a slower rate, where there were significantly less cells following 60 hours post-transfection of *DOCK5* siRNA where the mock population had reached 50% confluency. Furthermore, DOCK5 depleted cells took 32 hours more than mock transfected cells to reach confluence (Fig. 2a, e, Supplementary Figure 2a). Cells where CDC42 was depleted by siRNA also grew at a slower rate than mock (Fig. 2a, b). But cells lacking RHOA, RAC1, YAP, or TAZ grew at the same rate as mock transfected cells (Fig. 2a Supplementary Figure 2). However, the proliferation of cells simultaneously depleted of both YAP and TAZ was significantly impaired (Fig. 2a, Supplementary Figure 2). We conclude that DOCK5 and CDC42 promote proliferation of LM2 cells at least in part by promoting the nuclear translocation of both YAP and TAZ, though we cannot exclude the possibility that DOCK5 and/or CDC42 regulate proliferation independently of YAP/TAZ activation.

In order to determine if DOCK5 regulates survival in a fashion dependent on Rho GTPases, we assessed whether DOCK5 depletion is synthetically lethal with depletion of RAC1, RHOA, and CDC42. Indeed, DOCK5 and CDC42

exhibit synthetic lethality (Fig. 2b), such that at 156 hours from the start of the experiment, when mock transfected cells were confluent, cells with both CDC42 and DOCK5 knocked down were at 32% confluency. In contrast, depletion of either RAC1 or RHOA with DOCK5 partially rescued the lethality of DOCK5 depletion (Fig. 2c, d respectively). We conclude that DOCK5 exhibits genetic interactions with CDC42, RAC1, and RHOA, though the basis for the interaction with CDC42 is different than the interaction with RAC1 and RHOA.

LM2 cells harbour mutant KRAS (G13D)[72], which activates the kinases MEK and ERK, driving proliferation and survival[73,74]. However, while MEK inhibition (MEKi) effectively kills melanoma cells, it is largely ineffective in breast cancer cells[75,76]. In other cancer types, resistance to MEKi is due to YAP/TAZ activation[51,77,78]. Therefore we determined whether the resistance of LM2 cells to MEKi was due to DOCK5 and/or YAP/TAZ activity. To test this hypothesis we first treated LM2, MDA-MB-231 (from which LM2 cells are derived), and A375p melanoma cells (which harbour mutant BRAF) with the MEKi Binimetinib. MEKi significantly inhibited survival in MDA-MB-231 (Fig. 2e, f) and A375p (Fig. 2f, g) cells, but only had a modest effect in LM2 cells (Fig. 2f, h). DOCK5 depletion did not have any effect on the survival or proliferation of MDA-MB-231 or A375p cells in the absence or presence of MEKi (Fig. 2i, j). However, depletion of DOCK5 and MEKi treatment in LM2 cells led to a synergistic effect on proliferation or survival (Fig. 2h, g, i). Thus DOCK5 is essential for resistance of LM2 cells to MEKi.

DOCK5 depletion results in polarity and adhesion defects

We and others have shown that YAP/TAZ nuclear translocation is regulated by geometrical factors such as cell shape[32,33,42,60]. Thus we speculated that basal YAP/TAZ activation in LM2 cells, and decreases in nuclear YAP/TAZ in DOCK5 depleted cells might be a consequence of cell shape changes. Thus we sought to quantify how all RhoGEFs and RhoGAPs, and DOCK5 in particular contribute to cell shape determination in metastatic TNBC cells. Using high-content analysis, we quantified the cell shape of single LM2 cells following depletion of 149 RhoGEF/GAPs and 19 Rho GTPases to generate quantitative

morphological signatures (QMSs;[79]). In this case, QMSs describe the percentage of cells with a particular shape in an RNAi-treated population, and thus account for the phenotypic heterogeneity observed in different cell lines[80]. To generate QMSs, we used automated image analysis to extract 127 morphological and texture features, and trained linear classifiers capable of classifying cells into five visually distinctive reference shapes. The percentage of cells binned into each sub-population is a QMS for that specific RNAi (Methods). The five visually distinct shapes we used to characterize populations are: (1) 'spindly' - elongated cells with typically two protrusions; (2) 'large round'- spread cells of a large area which are often circular; (3) 'triangular' - cells with three distinct protrusions; (4) 'fan' - asymmetrically-shaped cells with nucleus to one side; and (5) 'small round' - cells which have a small area and high roundness (Fig. 3a,b). LM2 cells are highly heterogeneous, with a typical mock-transfected population displaying all of the shapes to varying degrees. For example, single cell quantification of shapes present in a mock-transfected well result in 6.1% cells classified as spindly, 1.1% as large round, 68.3% as triangular, 2.1% as fan, and 22.4% as small round (Fig. 3b, c). siRNA depletion results in a shift in these populations, where for example the top hit for spindly shape si*FAM13A* had 30.3% of cells classified as spindly, 0.2% as large, 50.9% as triangular, 1.7% as fan and 16.9% as small round (Fig. 3d).

As LM2s are highly heterogeneous we further developed a classifier for 'normal' cells (Methods, Supplementary Figure 3). This allowed us to identify siRNAs which had significant effects on cell shape based on whether they significantly depleted the percentage of normal cells compared to mock (Z-score equal to or below -1 for normal classifier). In essence we could thus describe the penetrance of each genetic perturbation. 89 siRNAs resulted in significant depletion of normal cells; of which 79 were RhoGEF/GAPs, 7 were Rho GTPases, and 3 were controls si*LATS1*, si*LATS2* and si*YAP1*.

To determine if cell shape regulates YAP/TAZ in LM2 cells, we next asked whether exemplars of different cell shapes that were used to derive classifiers had predictable variability in YAP/TAZ nuclear translocation. Effectively asking the question, does shape predict YAP dynamics? Indeed, different classifier

shapes had significantly different levels of nuclear YAP/TAZ ranging from high levels in polarized “fan” cells with broad lamellipodia to low levels in “spindly” cells (Fig. 3e, f). Thus as in other cell types[33–35,42,60], in LM2 cells morphology determines YAP/TAZ translocation dynamics.

To identify how different RhoGEFs, RhoGAPs, and Rho GTPases, and in particular DOCK5, regulate LM2 cell shape, we performed hierarchical clustering on 5-shape QMSs for shape hits (<-1 Z-score for normal classifier) in the LM2 OTP screen, and defined “phenoclusters” as genes grouped at the highest node of clustering with a Pearson Correlation Coefficient (PCC) of > 0.73 (Fig. 4a, Supplementary Table 2). This resulted in 10 multigene clusters and 1 singleton formed by mock transfected LM2 cells.

The QMS of DOCK5 siRNA belonged to cluster 8, and DOCK5 depletion has quantitatively similar effects to knockdown of: (1) CDGAP/ARHGAP31, a RhoGAP that localizes to FAs and regulates their dynamics during chemotaxis and durotaxis[81–83], as well as regulating the actin cytoskeleton in integrin-independent ways[84–86]; (2) PLEKHG3, an actin-binding protein that is essential for the establishment and maintenance of polarity in migrating cells[87]; and (3) the endocytic regulator INPP5B[88,89] (Fig. 4a). We propose that the shape phenotypes of cluster 8 are likely due to defects in cytoskeletal organisation and/or FA assembly at the leading edge of polarized migrating cells. Indeed, the QMSs of cluster 8 are correlated to both those of cluster 7 - whose most predominant member is the canonical polarity regulator CDC42[4,90–93] (Fig. 4a) and cluster 9 – which is characterised by very large flat cells which are indicative of defects in FA disassembly. Within cluster 8, only CDGAP/ARHGAP31 was a hit for low YAP/TAZ ratio in the OTP screen while PLEKHG3 and INPP5B had no effect (Supplementary Table 1).

We next asked whether the QMS of C21 treated cells is similar to that of DOCK5, YAP1, or LATS1 depleted cells. Because C21 inhibits GEF activity of DOCK5 towards RAC-type GTPases, we also asked whether it was similar to the QMS following knockdown of CDC42, RAC1, RAC2, RAC3, or RHOA. Hierarchical clustering of QMSs revealed that the QMS of C21 is most similar to

RAC2 and CDC42 depleted cells (Pearson Correlation Coefficient (PCC) > 0.77), but only partially similar to the QMS of DOCK5, YAP, and RAC3 depleted cells (PCC > 0.40) (Fig. 4b). Thus DOCK5 depletion is not phenotypically identical to disruption of DOCK5 GEF activity, and suggests that DOCK5 mediated regulation of shape occurs potentially both via GEF mediated regulation of RAC-type GTPase (i.e. RAC2), as well as by acting as a scaffold. That CDC42 knockdown mirrors the phenotype of C21 treatment, which suggests that CDC42 activation may be partially reliant on DOCK5 catalytic activation of RAC-type GTPases.

DOCK5 depletion reduces single cell invasion

To determine if DOCK5 contributes to the ability of LM2 cells to invade 3D tissues, we quantified the extent to which DOCK5 depleted cells invade rat tail collagen I (Col-I) gels.

Cells typically invaded from the bottom of the plate into depths of 30µM in the collagen gel within 24 hours (Fig. 5a, b). We quantified single-cell invasion by calculating the invasion index, defined as the number of cells at various planes within the gel divided by the total number of cells in said planes, plus the bottom plane. In a 2.0 mg/ml rat-tail Col-I gel, DOCK5 depletion significantly reduced invasion (Fig. 5c). Images in Fig. 5a-b show representative wells for each condition at a bottom plane and middle plane (0µM and 30µM respectively). Further, depleting TAZ but not YAP significantly reduced invasion, by the same amount as depleting DOCK5. This could suggest that it is TAZ that drives LM2 invasion rather than YAP. We propose DOCK5 promotes TAZ activation to promote shape changes that are required for 3D invasion.

Because collagen pore size has been shown to be inversely proportional to collagen concentration[94], we used collagen gels of different concentrations as a way of varying pore size. LM2 cells invaded regardless of pore size in the rat tail Col-I density range of 1.6 to 4.8 mg/ml, and depleting DOCK5 consistently reduced invasion across these concentrations (Fig. 5d). Overall these data suggest that DOCK5 is required for LM2 single-cell invasion in rat tail collagen

matrices independently of pore size, and we hypothesise that this decrease in invasion could be due to a lack of front rear polarity and consequent decreased YAP/TAZ ratio.

To explore whether DOCK5 is required for invasion of cells in multicellular bodies – i.e. in tumour models, we generated spheroids and quantified invasion into 100% Matrigel. Mock transfected LM2 cells invaded into the gel progressively after adding 100% Matrigel (Fig. 5e) forming radial branches, while cells lacking DOCK5 appear to just proliferate given the increase in diameter of the spheroid (Fig. 5f). Overall this suggests that LM2 cells require DOCK5 cell to invade into tissues from multicellular bodies.

DOCK5 depletion alters the levels of polarity proteins

In order to investigate how depletion of DOCK5 may affect YAP/TAZ localisation we carried out proteomic analysis on mock and si*DOCK5* transfected TNBC cell lines. Protein samples were processed 48 hours after transfection and labelled with TMT-10plex (Tandem Mass Tag) multiplex reagents before being submitted to LC-MS/MS (liquid chromatography mass spectrometry) (Methods). Protein abundance values obtained after analysis of mass spectra, were scaled within cell lines and the log2 ratio values of si*DOCK5* versus mock-transfected lines were calculated. DOCK5 protein was depleted by approximately 78% by siRNA (Fig. 6a, Supplementary Table 3). Further there were no changes in protein levels of DOCK5's closest homolog, DOCK1[95] (Fig. 6b), suggesting that the DOCK5 siRNA is not targeting DOCK1. In addition, there were no changes in protein levels of genes which clustered with DOCK5 by their QMS. Thus this confirms that DOCK5 siRNA has specific on-target effects.

Protein levels of Connective tissue growth factor (CTGF), which are upregulated by YAP/TAZ-TEAD activity[43,96] were significantly downregulated (log2 ratio: -0.77695) (Fig. 6a, Supplementary Table 3); supporting the idea that depleting DOCK5 renders YAP/TAZ cytoplasmic. Notably, total YAP and TAZ (encoded by the WWTR1 gene) protein levels remained unchanged (Fig. 6c), matching

our immunofluorescence data and confirming that DOCK5 regulates YAP/TAZ localisation rather than YAP/TAZ levels.

We performed hierarchical clustering on the abundance values of those proteins which were significantly upregulated (40% increase) or downregulated (40% decrease) upon DOCK5 depletion (log2 ratios above 0.5 and below -0.5 and permutation FDR <0.05 (false discovery rate) (t-test)). DOCK5 depletion resulted in changes in the levels of AKT effectors, AKT regulators, and proteins implicated in the establishment of front-rear polarity. Specifically, the protein levels of the AKT effectors GSK3β (log2 ratio: -0.58753) and FOXO3A (log2 ratio: -0.59131) were downregulated (Fig. 6a, c). GSK3β plays a role in the establishment of polarity where it has been described to be phosphorylated and inhibited at the leading edge of migrating cells in a mechanism dependent on integrin mediated activation of CDC42-PAR6-PKCζ[3,4,97]. Interestingly although it did not make the log2 ratio cut-off of -0.5 with a -0.46 log2 value, levels of the polarity regulator PAR6b were also substantially decreased (27%) in DOCK5 depleted cells ($p = 0.0002$, $q = 0.0008$). Finally, PHLPP2 which inhibits AKT[98] and aPKCζ[99], was upregulated (log2 ratio: 0.855787) (Fig. 6a, Supplementary Table 3). PHLPP2 upregulation has been shown to inhibit the establishment of polarity[99]. We conclude that depletion of DOCK5 results in decreased levels of signalling proteins and activity that maintain polarity and is consistent with the unpolarised shape of DOCK5 depleted cells (Fig. 4).

To validate the idea that DOCK5-RAC activity promotes the stability of GSK3β to promote polarity, we treated cells with C21 and measured total GSK3β at the membrane of migrating cells. C21 treatment significantly reduced GSK3β at the membrane in mock transfected cells to the same levels as just depleting DOCK5 by siRNA (Fig. 6d). We conclude that association of DOCK5 with RAC1 is required for the stability of GSK3β at the leading edge.

In order to test whether the decrease of GSK3β at the leading edge in DOCK5 depleted cells could be due to decreased AKT signalling, we treated cells with the AKT inhibitor Uprosertib (final concentration 2μM), and used LiCl (final

concentration 5mM) as a positive control of our ability to measure GSK3β phosphorylation (pGSK3β). We confirmed that Uprosertib indeed inhibits AKT by measuring FOXO3A nuclear translocation (Supplementary Figure 4a,b)[100,101].

LiCl caused an increase in pGSK3β levels at the membrane in mock-transfected cells, as expected based on previous studies, showing its inhibitory effect on direct inhibition of serine 9 on GSK3β and disruption of negative feedback of AKT by GSK3β[102], a phenotype exacerbated in DOCK5 cells (Fig. 6e). Further, we confirmed LiCl was working effectively by observing a significant increase in whole cell β-catenin levels via immunofluorescence (Supplementary Figure 4c, d) as previous studies have shown that LiCl-induced GSK3β phosphorylation results in β-catenin stabilisation[103–106], .

DOCK5 depleted cells significantly decreased pGSK3β[107], while AKT inhibition resulted in an even greater decrease in pGSK3β levels at the membrane in both mock and si*DOCK5* transfected cells (Fig. 6e).

In order to test whether YAP/TAZ translocation to the cytoplasm could be due to decreases in the levels of stable phosphorylated GSK3β at the membrane, and decreased AKT signalling, we quantified YAP/TAZ translocation following inhibition of AKT or GSK3β kinase activity, in both mock and si*DOCK5* treated cells. Inhibiting AKT directly with Uprosertib resulted in the same decrease in YAP/TAZ ratio in mock transfected cells as just depleting DOCK5 by RNAi (Fig. 6f). Furthermore, treating DOCK5 depleted cells with Uprosertib decreased the ratio significantly compared to mock transfected cells (Fig. 6f). LiCl however had no effect on YAP/TAZ. Thus AKT kinase activity, contributes to YAP/TAZ activation in LM2 cells.

Therefore these data suggest that DOCK5 is required for GSK3β stability at the leading edge and that the downstream pathway that leads to β-catenin stabilisation is unaffected[108] and is not involved in YAP/TAZ translocation. But

rather, we hypothesise that GSK3β stability at the leading edge as a result of DOCK5 signalling contributes to YAP/TAZ activation in these cells[97,109].

DOCK5 depletion reduces wound closure rates and affects Golgi orientation

To test our hypothesis that DOCK5 contributes to the establishment of front-rear polarity in migrating cells, we performed wound heal scratch assays, which are tests of polarity establishment, 2D migration speed, and migration persistence (Methods). We also examined whether DOCK5's activation of YAP/TAZ may be important for polarity establishment and migration. In these assays, we depleted DOCK5, YAP, TAZ, and YAP and TAZ in combination. Three time points from the 16 hr assays are shown in Fig. 7a for all conditions. Depleting DOCK5, TAZ, and YAP + TAZ significantly reduced migration rates (Fig. 7a, b), but depleting YAP did not. Thus, DOCK5 promotes migration in 2D.

The establishment of polarity during wound healing is characterised by the reorientation of the Golgi, and microtubule organising centre (MTOC), toward the wound area and direction of migration[107]. Therefore to determine if DOCK5 contributes to the establishment of leading edge polarity, we quantified the orientation of the Golgi following wounding, in cells at the edge of the wound[3,110]. Specifically, we quantified the angle of the Golgi oriented to the wound such that a 90 degree angle indicates the Golgi is facing toward the wound and front-rear polarity has been established (Fig. 7e, insert). Mock transfected populations had a high frequency of cells with Golgi directly facing the wound (65.8%) (Fig. 7c, di). In contrast, DOCK5 depleted populations had a higher frequency of Golgi oriented parallel to the wound (180 degrees) and or that were poorly polarised (35.4% to 17.7% respectively) (Fig. 7c, di). YAP and TAZ combined depletion resulted in the condition with the least percentage of cells displaying front-rear polarity (with Golgi oriented 90 degrees to the wound) and the highest percentage of cells with Golgi oriented 30 degrees relative to the wound, suggesting these cells are unable to integrate cues from the microenvironment for directional motility (Fig 7c, dii). Taken together, these data

support the idea that DOCK5 promotes the establishment of polarity in migrating cells.

DOCK5 depletion alters focal adhesion dynamics

We and others have demonstrated that DOCK5 localises in close proximity to FAs peripherally to Paxillin, but co-localises with Paxillin in the absence of GIT2[17,111]. In line with these data, we observed that overexpressed DOCK5-YFP is also localised in puncta at the very edge of the lamellipodial protrusions in TNBC cells. DOCK5 bordered the forward-facing side of Paxillin-positive FAs at the leading edge (Fig. 8a). Notably, the rear facing side of Paxillin-positive FAs at the leading edge was often bordered by polymerised alpha-tubulin.

To determine if DOCK5 has a role in FA dynamics in LM2 cells, we used Total Internal Reflection Fluorescence (TIRF) microscopy to visualise the recruitment of Talin-mApple to FAs in migrating mock and DOCK5 depleted cells. In mock cells small Talin-postive FAs form 0-4 µm from the leading edge in the lammellipodia of migrating cells (Fig. 8b and ci, adhesions coloured by FAAS software; Methods, Supplementary Video1). These FAs then enlarge/mature and turnover in the same region, and FAs are not stable in the lamella and/or cell body (Fig. 8cii – dynamics, Supplementary Video 1).

While migrating mock cells establish, and maintain, a polarised leading edge which is the site of both FA formation and turnover (Fig. 8ci and Supplementary Video 1), the changes in FA dynamics in DOCK5 depleted cells coincide with a failure of these cells to maintain polarity (Fig. 8cii and Supplementary Movie 2). Once established, the leading edge in randomly migrating control cells is maintained for approximately 120 min. In DOCK5 depleted cells there is rarely only one leading edge at any given time but rather many protrusions lasting approximately 40 minutes on average (Supplementary Video 2).

We quantified the assembly and disassembly dynamics of individual FAs in mock and DOCK5 depleted cells. We used a Cumming estimation plot to demonstrate the mean difference in the assembly and disassembly rates and phase lengths. Effect sizes based on Cohen's initial suggestions[112,113] indicate that values of 0.2 to 0.5 are small, 0.5 to 0.8 are medium, 0.8 to 1.2 are large, and 1.2 to 2.0 are very large effect sizes. In DOCK5 depleted cells, FAs have significantly accelerated assembly and disassembly rates compared to control FAs (Fig. 8d, orange unpaired Hedges' g of 1.65; red unpaired Hedges' g of 1.28). But notably, despite accelerated disassembly rates, FAs in DOCK5 depleted cells often fail to completely turnover (Fig. 8b, c) and assembly and disassembly phase lengths were largely unaffected (Fig. 8e, Hedge's g of 0.101 and -0.0986 for assembly and disassembly phase lengths respectively).

The most parsimonious explanation for these observations is that in the absence of DOCK5, FAs can be rapidly stabilised but also results in failure to turnover (Fig. 8cii). Despite impaired turnover, FAs in DOCK5 depleted cells are highly unstable and exhibit fast shrinkage rates, potentially because actin-mediated force maturation is impaired in DOCK5 depleted cells. This model is consistent with the observation that lamellipodia are highly unstable in DOCK5 depleted cells (Supplementary Video 2).

CDC42 and RHOA depletion affect FA morphogenesis in metastatic cells

We investigated whether the defects in FA morphogenesis following DOCK5 depletion were due to decreased DOCK5-mediated RAC activation, or whether DOCK5 regulates FA morphogenesis in RAC-independent ways. We first knocked down RAC1, RHOA, and CDC42 and measured Talin-mApple dynamics in migrating LM2 cells (Fig. 9a). We also measured FA dynamics following treatment with Uprosertib to determine the effect of AKT signalling on FA morphogenesis.

Depleting CDC42 significantly accelerated assembly rates (Hedges' g: 0.851) in a similar manner to DOCK5 depletion, and large FAs formed rapidly (Fig. 9b). However, all other aspects of FA morphogenesis including disassembly rates

(Fig. 9c), the length of assembly (Fig. 9e), stability (Fig. 9d), and disassembly phase length (Fig. 9f) were largely unaffected.

In contrast, RAC1 depletion increased the length of the assembly phase (Fig. 9e); consistent with the role of RAC1 in promoting FA maturation[114]. While RHOA depletion resulted in a significant increase in FA disassembly rates (Fig. 9c), in line with the idea that inhibition of RHOA mediated contractility results in unstable adhesions. Uprosertib treatment resulted in similar effects as RHOA inhibition, as FAs had high disassembly rates, indicative of unstable adhesions (Fig. 9c). However the effect on FA morphogenesis based on all other metrics following depletion of RAC1 and RHOA, or following Uprosertib treatment, was relatively mild.

Taken together these data suggest that CDC42 inhibits FA growth and turnover, RAC1 promotes growth, while RHOA and AKT promote maturation and turnover. Interestingly, DOCK5 depletion appears to have much broader effects on FA morphogenesis than any single Rho GTPase alone suggesting it acts upstream of all Rho GTPases – either directly as a GEF or indirectly - in the control of FA growth, maturation and turnover. Further, AKT inhibition closely mimics that of RHOA, suggesting AKT functions in the late stages of FA maturation.

DOCK5 and CDC42 stabilise polarity

We next sought to explore the idea that DOCK5 acts to modulate a CDC42-GSK3β axis that stabilizes MTs at the leading edge of protrusive cells to reinforce the establishment of polarity. Cells were plated on fibronectin (FN) and fixed after 3 hours. After 3 hrs, spreading LM2 cells establish a single leading edge adhered to the matrix by stable FAs, and thus have an asymmetric morphology (Fig. 10) However, in line with both our high-content imaging data (Fig. 4) and live cell data (Fig.8), after 3 hrs of spreading, DOCK5 depleted cells established multiple smaller protrusions, leading to asymmetric shapes (Fig. 10). Paxillin-positive FAs in DOCK5 depleted cells were very small and appeared diffusely spread in the leading edge. Consistent with previous reports

demonstrating a role of DOCK5 in promoting MT stability[115,116], there were dramatically fewer MT bundles in the periphery of DOCK5 depleted cells, and MTs appear thin and poorly organized compared to those of mock transfected cells.

CDC42 depletion led to a partially similar phenotype as that of DOCK5, as cells formed expanded lamellipodia that nearly encompassed the entire circumference of the cells, and adopted a rounded, symmetric shape (Fig. 10). As in DOCK5 depleted cells, Paxillin-positive FAs in CDC42 depleted cells appeared small and diffusely spread throughout the protrusion. In contrast, cells depleted of RHOA, or RAC1+RAC2 all formed polarised lamellipodia with multiple large FAs (Fig. 10). Treatment of cells with either FAKi or Blebbistatin did not inhibit the formation of polarised lammelipodia, although no FAs formed in Blebbistatin treated cells (Fig. 10). These data demonstrate that DOCK5 and CDC42 act to promote the stability of polarised leading-edge lammelipodia, and FA stability.

DOCK5 promotes spreading following MT depolymerisation

To investigate the relationship between MTs and DOCK5 at the leading edge, we performed assays to analyse cell morphology following washout of the MT-depolymerization agent nocodozole (NZ) in media containing either: NZ, the MT-stabilising agent taxol (TX) or DMSO. After NZ treatment, all cells became round and poorly adhered (Fig. 11a, b). 30 minutes after washout in DMSO containing media, control cells formed abundant filopodial protrusions increasing in cell area ($p = 0.013$) likely as a result of MT outgrowth and RAC1 promoting actin polymerisation[117,118]. Indeed, actin intensity at the membrane significantly increased in DMSO washout for mock transfected cells denoting actin polymerisation (Fig. 11e). On the other hand, while actin intensity at the membrane was also significantly increased in DOCK5 depleted cells (Fig. 11e), they failed to spread and increase in cell area under DMSO containing media washout (Fig. 11b, e, $p = 0.013$ for mock, $p = 0.0894$). This would suggest that while there may be some actin polymerisation, MT outgrowth is not occurring. Further, tubulin organisation as denoted by SER Ridge (texture feature) was

significantly different in DOCK5 depleted cells compared to mock under both control conditions (DMSO only) (Fig. 11c) and NZ treatment and washout in NZ (Fig. 11c).

Washout in TX containing media on the other hand resulted in a significant increase in cell area for both mock and DOCK5 depleted cells (Fig. 11a,b, $p < 0.0001$ for mock, $p = 0.001$) likely as a result of MT stabilisation. Indeed, TX washout resulted in changes in tubulin texture (SER Ridge) resembling those of control conditions (Fig. 11c). Thus stabilising MTs rescues many of the phenotypes associated with DOCK5 depletion. Further, actin intensity at the membrane was significantly increased in both mock and DOCK5 depleted cells in TX washout, indicative of actin polymerisation (Fig. 11e, $p = 0.0076$). DOCK5 depleted cells did not display polarised fronts for any condition supporting our hypothesis that DOCK5 is required for maintenance of polarity.

Overall these data suggest that DOCK5 depleted cells have impaired MT outgrowth and MT instability, as well as decreased RAC1 activity promoting actin polymerisation, supporting our hypothesis that DOCK5 couples MT stability machinery with FA to promote polarity in migrating and spreading cells.

Discussion

In both yeast and mammalian cells the recruitment and activation of CDC42 at the membrane serves to seed polarised cortical structures that are enriched complexes and cytoskeletal elements that would otherwise be diffusely or asymmetrically organized in cells[119]. Such structures lead to cells that have a “front” and “back”. During the formation of the bud in *S. cerevisiae*, localised CDC42 activation marks the site of bud assembly at one site on the membrane[120,121]. A key aspect of bud morphogenesis are positive feedback loops initiated by CDC42 which increase the local concentration of GTP-bound and active CDC42 [122]. One effect of these loops is that one bud site outcompetes all other potential sites for the recruitment of bud assembly in a “winner takes all” fashion[123,124]. Indeed in genetic mutants where the

reinforcement, but not necessarily the establishment, of polarity is disrupted, multiple bud sites form[124,125].

In the case of migrating mammalian cells, the establishment of polarity occurs with the coincident reorganisation of the actomyosin cytoskeleton to generate protrusions such as lamella and lamellipodia, and the engagement of the ECM by integrins to form FAs[126]. Classical studies have shown that CDC42 regulates microtubule stability and establishment of polarity via PAR6 and PKCζ mediated phosphorylation of GSK3β at the leading edge of migrating cells in a manner that is integrin dependent[3,4,97]. Here we propose that DOCK5 acts at FAs in breast cancer cells to establish positive feedback loops which maintain polarity in the presence of stable integrin-ECM attachments and cellular tension. By reinforcing polarity in sub-cellular regions with stable FA attachments, DOCK5 promotes processive migration and 3D invasion (Fig. 12). We and others have previously observed that DOCK5 is recruited to FAs[17,111]. We show that DOCK5 acts to couple FA morphogenesis and polarity by coordinating multiple GTPase activities. Firstly, DOCK5 acts as a GEF for RAC-type GTPase to promote FA assembly and ultimately maturation/turnover. In the absence of DOCK5, FAs do not increase in size, and the turnover of existing FAs is disrupted (Fig. 8) likely because of a failure of DOCK5-depleted FAs to engage actin at the leading edge[5,126,127]. Failure to mature FAs and/or engage actomyosin likely results in decreases in RHOA activation (Fig. 12). Secondly, by recruiting and activating AKT to FAs near the leading edge, DOCK5 stabilizes GSK3β, which is targeted by CDC42-PKCζ for phosphorylation, leading to the maintenance of polarity. In cells depleted of DOCK5, CDC42 activation at the membrane, the initial establishment of polarity, is not initially affected. But either C21 treatment or lack of DOCK5 reduces the levels of GSK3β that can be phosphorylated by CDC42-PKCζ, leading to a failure of cells to maintain polarity. CDC42 activation (which is initially independent of DOCK5) at another subcellular site can lead to formation of a new unstable leading edge in other regions of the cells. Indeed, a characteristic of DOCK5 depleted cells is not the ability to form protrusions, but rather to maintain a stable polarised protrusion. As such this phenotype is highly reminiscent of *rdi1* and *bem1/2* yeast mutants which form numerous unstable buds[122,124,125].

Critically, by promoting FA assembly DOCK5 initiates different positive feedback loops. In one loop, more DOCK5 activity at FAs leads to further DOCK5; promoting FA assembly, and ultimately turnover. In a second loop, more DOCK5 increases the levels of AKT which promotes further GSK3β stability and phosphorylation (Fig. 12). Finally, DOCK5 could potentially mature FAs to recruit CDC42 GEFs which can further amplify CDC42 activation at the leading edge. Indeed depletion of CDC42 GEFs FGD5 and PLEKHG3[87,128] results in similar morphological changes as DOCK5 depletion (Fig. 4). FGD5 has been previously shown to regulate polarity downstream of Rap1 GTPase [128], and thus could serve an orthologous function to yeast CDC24 RhoGEF which is activated by Rap1 signalling to promote CDC42 positive feedback at the bud scar[122].

DOCK5 has been previously described to recruit and activate AKT and promote GSK3β phosphorylation through both RAC-dependent and independent ways[115,116]. In particular, DOCK5's C-terminus has been shown to recruit NCK/AKT complexes to promote GSK3β phosphorylation in ways that are independent of catalytic activation of RAC-type GTPase through its DHR2/GEF domain[115,116]. But our observation that the DOCK5 GEF inhibitor C21 mimics the effect of both DOCK5 siRNA and AKT inhibition by Uprosertib on GSK3β localisation at the membrane and YAP/TAZ translocation strongly suggests that DOCK5 mediated activation of RAC-type GTPases via its DH2/GEF is required for GSK3β phosphorylation and localisation at the leading edge. One model which resolves these previously contradictory observations is that activated DOCK5 exists in a conformation that recruits NCK and AKT to its C-terminus independent of it GEF domain; but also functions as a GEF to promote RAC-mediated FA assembly – which recruits more DOCK5/NCK/AKT to FAs in a positive feedback loop. Thus inhibition of RAC by C21 breaks this loop and lowers AKT activation. Our observation that AKT inhibition by Uprosertib mimics different aspects of DOCK5 depletion on FA morphogenesis in fact suggests that AKT activity itself promotes FA morphogenesis and is involved in this positive feedback loop (Fig. 12).

We and others have previously demonstrated that YAP/TAZ nuclear translocation is dependent on cell shape and geometry[33–35,42,60]. Our data suggest that decreases in YAP/TAZ nuclear translocation in DOCK5 are due to the inability of DOCK5 depleted cells to maintain a polarised, adherent morphology leading to low YAP/TAZ. Mechanistically this can be explained by the inability of cells to assemble stable FAs (Fig. 8). The absence of fully mature FA leads to both defects in assembly of complexes at FA which promote YAP/TAZ activation – i.e. via signalling pathways such as PAK2[42] or FAK-PI3K[129] and/or the failure of FAs in DOCK5 depleted cells to engage actin and upregulate actomyosin contractility[1,2] which promotes YAP activation[130].

It is tempting to speculate that sustained YAP/TAZ nuclear translocation, and resulting capabilities such as drug resistance, may be a consequence of cancer cells adopting stable polarised migratory forms. In the case of LM2 cells, the idea that processive migratory forms driven by DOCK5 activity leads to shape changes which then drive YAP/TAZ activity and cancer relevant phenotypes such as drug resistance, is further supported by the finding that across genetic backgrounds (different RNAi perturbations) shape is predictive of YAP/TAZ activity (Fig. 3e,f). This model would be in contrast to the classical idea that drug resistance and migration are coincident events, and/or that YAP/TAZ itself drives migration. Indeed, studies in melanoma cells have shown that YAP/TAZ upregulation which promotes drug resistance is caused by shape changes[47,49,57,58]. Moreover, a number of recent studies have shown that EMT in breast cancer, which is characterized by morphological changes and increased invasive capabilities, also leads to drug resistant cells[131]. Thus shape changes may be causal to many aspects of TNBC, and suggests that therapeutic intervention could occur by preventing cells from altering their shape.

Materials and Methods

Cell culture

LM2s (subpopulation 4172 from MDA-MB-231) were obtained from Joan Massagué (Sloan Kettering Institute, New York)[31], and stably express a triple-fusion protein reporter construct encoding herpes simplex virus thymidine kinase 1, green fluorescent protein (GFP) and firefly luciferase (Minn et al., 2005). MDA-MB-231 cells were obtained from Janine Erler (University of Copenhagen, Denmark), while SUM159 and hs578t were a gift from Rachel Natrajan (Institute of Cancer Research, London). Cells were grown in Dulbecco's Modified Eagle Medium (DMEM) supplemented with 10% heat-inactivated fetal bovine serum (FBS) and 1% penicillin/streptomycin in T75 falcons, at 37°C and supplemented with 5% CO_2 in humidified incubators. MCF10A were obtained from ATCC and were grown in DMEM/F12 supplemented with 5% horse serum, 10µg/ml insulin, 20ng/ml epidermal growth factor, 100ng/ml cholera toxin, 500ng/ml hydrocortisone, and 100mg/ml penicillin/streptomyocin in T75 falcons.

T47D were obtained from from Rachel Natrajan (ICR), and were grown in Roswell Park Memorial Institute (RPM1)-1640 culture medium (Gibco) supplemented with 10% heat-inactivated fetal bovine serum (FBS) and 1% penicillin/streptomycin in T75 falcons.

siRNA transfections

All siRNAs were made up to a stock of 20µM. Briefly, for 384 well plates, siRNA reverse transfections were performed by adding 40nL of siRNA to each well followed by 5µl of Opti-MEM® Reduced Serum Media. 5 minutes later 5µl of mix containing Opti-MEM and RNAimax reagent in a 125:1 ratio were added per well. Plates were spun at 1000 rpm for 1 minute, and incubated at room temperature for 20 minutes to allow siRNA-RNAimax complexes to form. Cells were plated on top in 30µL of DMEM (10% FBS, 1% penicillin/streptomyocin), resulting in a total volume of 40µL per well: 40nL siRNA (final concentration of 20nM), 5µL Opti-MEM, 5µL of Opti-MEM and RNAimax mix (125:1) plus 30µL of cells. For transfections performed on 96 well plates and 6 well plates, 4 and 64 times the amounts used for 384 well plates were used, respectively. When siRNAs were transfected in combination, the same amount of each siRNA was used. siRNAs and sequences used can be found in Table 1.

Table 1: siRNA target sequences

siRNA	Sequences	Catalogue number
DOCK5 OTP pool	GAGGAGAGAUUGUUAAGUU, GAACAUUAAACACAACCUA, GCAAAUUCAUUCAAAGCAU, GGGUUGCGAUCUAUAACUA	# L-018931-00-0005
DOCK5 OTP pool deconvoluted (5-8)	GAGGAGAGAUUGUUAAGUU, GAACAUUAAACACAACCUA, GCAAAUUCAUUCAAAGCAU, GGGUUGCGAUCUAUAACUA	# LU-018931-00-0002
DOCK5 siGENOME pool deconvoluted (1-4)	AGAACUAUCUAAUUCGUUG, GUAACGGGAUGCCCAAGGA, GAGUGGCAGUGAUGGAUAU, UAUCAUACAUGGGAAGGUG	# MU-018931-01-0002
YAP OTP pool	GCACCUAUCACUCUCGAGA, UGAGAACAAUGACGACCAA, GGUCAGAGAUACUUCUUAA, CCACCAAGCUAGAUAAAGA	# L-012200-00-0005
WWTR1 (TAZ) OTP pool	CCGCAGGGCUCAUGAGUAU, GGACAAACACCCAUGAACA, AGGAACAAACGUUGACUUA, CCAAAUCUCGUGAUGAAUC	# L-016083-00-0005

LATS1 OTP pool	GGUGAAGUCUGUCUAGCAA, UAGCAUGGAUUUCAGUAAU, GGUAGUUCGUCUAUAUUAU, GAAUGGUACUGGACAAACU	#L-004632-00-0005
LATS2 OTP pool	GCACGCAUUUUACGAAUUC, ACACUCACCUCGCCCAAUA, AAUCAGAUAUUCCUUGUUG, GAAGUGAACCGGCAAAUGC	#L-003865-00-0005
RHOA OTP pool	CGACAGCCCUGAUAGUUUA, GACCAAAGAUGGAGUGAGA, GCAGAGAUAUGGCAAACAG, GGAAUGAUGAGCACACAAG,	# L-003860-00
RAC1 OTP pool	GUGAUUUCAUAGCGAGUUU GUAGUUCUCAGAUGCGUAA AUGAAAGUGUCACGGGUAA GAACUGCUAUUUCCUCUAA	# L-003560-00
RAC2 OTP pool	UGACAACUAUUCAGCCAAU CCAAGGAGAUUGACUCGGU CCAAGUGGUUCCCAGAAGU UGAAAACCGUGUUCGACGA	# L-007741-00
RAC3 OTP pool	AAACUGACGUCUUUCUGAU ACAAGAAGCUGGCACCCAU GAAGACAUGCUUGCUGAUC CGUGAUGGUGGACGGGAAA	# L-008836-00
CDC42 OTP pool	CGGAAUAUGUACCGACUGU GCAGUCACAGUUAUGAUUG GAUGACCCCUCUACUAUUG CUGCAGGGCAAGAGGAUUA	# L-005057-00

Plasmid transfections

For transfections with Talin mApple and DOCK5-GFP, Effectene Transfection Reagent (Qiagen) was used according to manufacturer's protocol. Cells were plated at a density of 1.0 x 10^6 cells /ml in 1ml in a 6 well plate. Then, 2.56ng of plasmid were combined with 150µl of EC buffer and vortexed followed by addition of 8µl of Enhancer and vortexing. After 10 minutes 5µl of Effectene were added, mix was vortexed, 10 minute later 1ml of DMEM was added and mixture was dispensed dropwise per well. If siRNA was used as well, cells were reverse transfected as usual. Experiments were performed 48 hours later.

Generation of CAAX-GFP tagged cell line

CAAX-GFP tag was a kind gift from Nicola Ferrari (previously Institute of Cancer Research, currently Astex Pharmaceuticals, UK), who generated it in HEK-293 cells using a second-generation lentiviral vector (plasmid EGFP-CAAX pCSII-IRES2-hygro). Cells were plated at a density of 6.4 x 10^4 cells /ml in a 6 well plate. Cells were transfected 24 hours later using a 1:1 dilution of lentivirus containing the CAAX-GFP tag solution and DMEM per well according to the manufacturers protocol. Transfected cells were selected with Hygromycin B (Invitrogen, cat # 10687-010) at a final concentration of 500µg/ml (elucidated from carrying out a concentration curve) 72 hours post transfection. CAAX tag did not affect YAP/TAZ ratio or cell morphology.

Drug treatments

Drugs were usually added on top of media already present. Appropriate amounts of DMSO or H_2O depending on what the drug was dissolved in were added to mock transfected cells. A list of drugs used can be found in Table 2. Drugs were added for a period of 4 hours, unless other stated, so as to eliminate any cell cycle effects.

For the nocodazole and taxol experiment, cells were mock and si*DOCK5* reverse transfected as described in RNAi screening methodology for 48 hours. Then, cells were trypsinised and plated at a density of 1500 cells/well and allowed to settle for 20 hours. Microtubule polymerisation was induced by nocodazole at a final concentration of 10µM for 4 hours. Washout was performed for 30 minutes in either DMSO, 10µM nocodazole, or 10µM taxol – containing DMEM as indicated in Fig 11.

Table 2: Drugs added.

Drug	Inhibitor type/target	Company and catalogue number	Final concentration.
PF-573288	FAK inhibitor	Tocris Biosciences, #3239; CAS 869288-64-2	2µM
C21	DOCK5 inhibitor	Alfa Aesar,	100µM

		#H60031.MD; CAS 54129-15-6	
Blebbistatin	Myosin II light chain	Sigma, #B0560; CAS 856925-71-8	10µM
Uprosertib (GSK2141795)	AKT inhibitor		2µM
Taxol (Paclitaxel)	Microtubule stabiliser	Sigma, #T7181	10µM
Nocodazole	Microtubule depolymeriser	Sigma, #M1404	10µM

RNAi screening methodology

40nl (0.08pmol) of siRNA from an ONTARGET*Plus* human siRNA RhoGEF/GAP and Rho GTPase library (stock concentration of 20µM, Dharmacon) were arrayed using the acoustic liquid handler Echo 550 prior to transfection and kept at -80°C. All siRNAs were arrayed in duplicate per plate and each plate was arrayed in duplicate resulting in a total of 4 plates per library. Pre-stamped siRNA plates were thawed at room temperature for 30 minutes prior to use. 5µl of Opti-MEM® Reduced Serum Media were then added per well followed by 5µl of RNAiMax reagent (Invitrogen) and Opti-MEM® mix in a 1:125 ratio. Plates were spun down at 1000 rpm for 1 min and incubated at room temperature for 20 mins. Cells were then seeded at a concentration of 30000 cells/ml in 30µl DMEM supplemented with 12.8% FBS, 1.28% penicillin/streptomyocin (10% FBS and 1% penicillin/streptomyocin final) to account for the 10 µl of mix already present in the well, resulting in a total volume of 40µl per well. Automated handling of plates on the Cell::Explorer robot station was carried out using the PlateWorks software (Perkin Elmer). Plates were fixed 48 hours later with 8% warm formaldehyde in PBS (final concentration 4%) for 15 minutes and permeabilised with 0.1% Triton-X-100 in PBS for 10 minutes. Cells were then blocked in 2% BSA in PBS for 2 hours. All antibody incubations were performed in solution containing 0.5% BSA, 0.01% Triton-X-100 dissolved in PBS in a 1:1000 ratio, with the first primary antibody being added overnight at 4°C and the rest being incubated at room temperature

for 1.5 hours. Plates were washed 3x with PBS between every step using a Microplate Washer (BioTek). Antibodies were added sequentially to prevent cross reactivity. Antibodies used were: mouse YAP/TAZ (Santa Cruz Biotechnologies, cat # sc-101199), rat α -tubulin (Bio-Rad, cat # MCA77G), AlexaFluor 647 goat anti-mouse (Life Technologies, cat # A21235), AlexaFluor 647 goat anti-rat (Life Technologies, cat # A11077), phalloidin (Invitrogen, cat # A12379). Finally Hoechst (Sigma Aldrich, cat # 33258) was added for 15 minutes, and after washing, cells were left in PBS and plates were sealed. Cells were imaged using an automated Opera Quadrupule Enhanced High Sensitivity (QEHS) spinning-disk confocal microscope (Perkin Elmer) with 20x air lens. 28 fields of view were imaged per well. Cells were plated at increasing densities on columns 1, 2, 23 and 24 to be able to account for density dependent effects.

Images were processed and analysed using Columbus 2.6.0. Software Platform (PerkinElmer). Briefly, single cells were identified using the nuclear Hoechst signal. α-tubulin intensity was using to segment the cytoplasm. Cells touching the image border were filtered out. Following this, cell morphology and texture features were extracted from all stains as described extensively in Pascual-Vargas et al, *Scientific Data* 2017. In the same script, a cell shape linear classifier was manually trained on visually distinctive cells that represented each category (spindly, large round, triangular, fan, and small and round) and included all the features extracted from the stains except those based on YAP/TAZ. YAP/TAZ ratio was calculated as log ratio of nuclear to ring region (perinuclear region) and was not included in the classifier. The percentage of cells classified into each shape was calculated per well and normalized per plate. Z-scores were then calculated per screen using the average and standard deviation of all mock transfected cells. Each well was assigned a QMS consisting of the Z-score for each shape.

Because we have previously observed that following efficient gene depletion, many cells in a population can appear wild-type[80], which can potentially obscure the presence of phenotypes resulting from gene depletion, we identified and filtered normal cells from our data set in the following way. Briefly, we performed principal component analysis (PCA) on single cell dataset comprised of texture

and morphological features of populations which were either mock transfected or transfected with siRNAs which scored the highest for enriching for a particular shape. The data were projected into 2D PC space and each data point (cell) colour coded by the shape of each cell (Supplementary Figure 3a). We defined the region of shape space where different classified cells overlapped in PC space as normal cells, defined as those whose PC coordinates lay within 1 SD of the mean of PC1 and PC2 for the siRNA transfected population (black box, Supplementary Figure 3b). We trained the new linear classifier on the cells that fell in this space in the mock transfected population (black box, Supplementary Figure 3a) and defined this population as 'normal'. Running the classifiers again on the same data, performing the same PCA analysis on this new dataset and removing cells classified as 'normal' resulted in cells classified into the different shapes separating better in PC shape space (Supplementary Figure 3c). Further analyses are described in the results section.

Quantitative Real-Time PCR (qRTPCR)

RNA was extracted using phenol:chloroform (TRIzol®, ThermoFisher cat # 15596026) and RNAeasy kit (Qiagen cat # 74104) according to the manufacturer's protocol. RNA was converted to cDNA using a cDNA conversion kit (Applied Biosystems cat # 4387406) according to the manufacturers protocol. qRTPCR was performed on a QuantStudio® Flex Real-Time PCR system, using PCR mastermix SyBR green (Applied Biosystems cat # 4309155) and primers in Table 3.

Table 3: PCR primers used for qRT-PCR.

Gene	**Forward (5'-3')**	**Reverse (5'-3')**
DOCK5	GCTTTGAACTTCAGCTCTGG	CCACATGTCCCGGATTCTAA
WWTR1/TAZ	TATGGGACAGTCCGGGAGC	CGAGGCTTGGCTGACAAATC
YAP1	GACTTCCTGAACAGTGTGGA	CAGCCAAAACAGACTCCATG
GAPDH	AGATCCCTCCAAAATCAAG	GGCAGAGATGATGACCCTT

3D collagen invasion assay

We chose rat tail Col-I as our matrix because it is the most abundant type of collagen in mammalian tissues[132–136], and has been shown to form networks with physiological mechanical properties *in vitro*[137,138139].

Cells were reverse transfected in 6 well plates as previously described. 48 hours later cells were trypsinised and resuspended in a solution containing rat-tail collagen I (Corning cat # 354249), ultrafiltered H_2O (prepared in house according to standard protocols), DMEM 5x and HEPES (1M pH 7.5, prepared in house according to standard protocols). Collagen solutions were prepared on ice and 96 well plates were prechilled prior to use. Collagen solutions were made up as in Table 4 starting with HEPES, followed by DMEM 5X with rat-tail collagen being added last. Neutralisation of collagen was tested with pH strips prior to use to ensure a pH of 7.4. DMEM 5X was made up using 12.5g DMEM powder, 25 ml of 1M HEPES ph 7.5, 5g $NaHCO_3$**,** H_2O up to 250 ml and was filtered under sterile conditions before aliquoting into 10ml batches and freezing them at -20°C. Cells were spun down in 1.5ml eppendorfs at 1000 rpm for 4 minutes, and supernatant was removed. Cell pellets were resuspended carefully so as to not introduce bubbles in 500µL of collagen solution, and 100µL of cell-collagen mix was dispensed per well of a 96 well plate. Once all conditions were dispensed, plates were spun down for 1 minute at 4 °C to ensure all cells were at the bottom of the plate. Collagen was allowed to polymerise at 37°C for one hour. Then 50µL of DMEM were added on top of the collagen gels. 150µL of PBS were added to all outside wells to prevent gel dehydration and edge effects due to dehydration. Cells were fixed 48 hours later with 50 µL/well of 16% PFA containing Hoechst (1:500) for 2 hours. Gels were then washed with PBS and left in PBS prior to sealing. The Opera QEHS spinning-disk confocal microscope (PerkinElmer) with 20x air lens was used to image these plates. A minimum of three Z stacks were taken per well, spaced 30µm apart with 0µm referring to the bottom of the plate and subsequent stacks referring to inside the gel. 20 fields were imaged per well per stack, and were all in the centre of the well to prevent edge effects. Columbus software was used to quantify cell number at every stack, using a filtering threshold method to

ensure only cells with a certain nuclear and GFP intensity were counted in each stack (Supplementary Figure 5).

Table 4: Reagents used for collagen invasion assays.

	Stock	Final concentration
Rat-tail collagen I	10.31 mg/ml	2.0 mg/ml
UF H_2O (cold)	-	remaining
DMEM 5x	5x	1x
HEPES 1M pH 7.5	100%	2%

Spheroid invasion assay

Cells were reverse transfected in 96 well ultra-low attachment (ULA) plates as described in the siRNA transfections section. Quantities used per well: 20 µl OPTIMEM + 0.16 µl RNAimax, 20 µl OPTIMEM + 0.16 µl siRNA. Cells were plated at a density of 4.0 x 10^4 cells/ml in 120µl, resulting in a final volume of 160µl per well. Due to their mesenchymal nature, LM2 cells required 2% Matrigel in ultra-low attachment plates to form spheroids, therefore 5 hours later a solution of 2.5% Matrigel in 40 µl of DMEM was added per well to promote spheroid formation resulting in a total volume of 200µl per well. 48 hours later 180µl of medium was carefully removed from each well so as not to disturb the spheroid, and replaced with 180µl of 100% Matrigel. Spheroids were imaged prior to adding 100% Matrigel and immediately after using the Celigo Imaging Cytometer (Nexcelom Bioscience). Spheroids were imaged every day for 8 days, following the protocol outlined in [140]. Images were processed using ImageJ. Invasion area was determined by drawing a circle to the edge of where cells invaded and subtracting the initial area of the spheroid at day 0. Proliferation was quantified by drawing a circle around the edge of the area of the spheroid where the spheroid is grey, rather than the edge, so as to exclude any invading cells.

Western blotting

Cells were reverse transfected in 6 well plates at a density of 3.3 x 10^4 cells /ml in a 6 well plate (same density as screens and all other experiments unless otherwise stated) for 48 hours. Cells were harvested by trypsinising, spinning down in 1.5ml eppendorfs and removing supernatant. Cells were then washed in PBS 3 times. Pellets were then resuspended in 500µl of solution containing a ratio of 3:1 of water to LDS Sample Buffer (4x) (Invitrogen) with a final concentration of 2mM DTT. Samples were then boiled at 100 C for 10 minutes and spun down for 2 minutes at 13 000 rpm. Samples were frozen at -20°C. Samples were boiled and spun down again prior to use. 16µl of sample were loaded into 1.0mm 15 well pre cast Novex 4-20% Tris-Glycine Gels (Invitrogen #XP04205BOX) and 30µl into 10 well pre cast gels. Ladder used was Color Protein Standard, Broad Range (11-245 kDa) (New England Biolabs, #P7712S). Lysates were run in 1x Tris-Glycine (Thermo) running buffer at 130V until the bands reached the bottom of the gel. Gels were transferred in transfer buffer at 4°C at 0.2 A onto a methanol activated polyvinylidene fluoride (PVDF) membrane (Immobilon-FL). Membranes were then stained with Ponceau (Sigma) dissolved in acetic acid to ascertain where the proteins were before cutting the membrane at required places. Membranes were then blocked in either 5% milk (Marvel) or 5% BSA if staining for phospho-proteins in Tris-buffered saline (TBS, prepared in house according to standard protocols) 0.1% Tween20 (TBST) solution for 1 hour at room temperature (RT)on a rolling shaker. Membranes were then washed once in TBST. Primary antibodies were diluted in either 5% milk TBST or 5% BSA TBST solution and incubated at 4°C overnight on a rolling shaker. 10% glycerol was added to primary antibody solutions to be able to reuse them post storing at -20°C. Membranes were washed 3 x 15 minutes in TBST. Membranes were then incubated for one hour at RT in either appropriate (mouse or rabbit) Horse radish peroxidase (HRP) -linked secondary antibodies (Cell Signaling) in TBST for chemiluminescent detection. Membranes were washed 3 x 5 minutes with TBST. Membranes were treated with ECL substrate (Thermo, #32106) and exposed using Azure Biosystems c600 western blot imaging system. Descriptions of antibodies used and dilutions can be found in Table 5. Western Blots were quantified using Image J and normalised to GAPDH unless otherwise stated.

Subcellular fractionation

Thermo's Subcellular Protein Fractionation Kit for Cultured Cells (#78840) was used according to the manufacturer's protocol to extract cytoplasmic, membrane, nuclear soluble, chromatin-bound and cytoskeletal proteins. Briefly, cells were harvested by trypsining them and centrifuging for 5 minutes. Cell pellets were washed with ice-cold PBS. Cells were counted so as to be able to use the corresponding ratios of Cytoplasmic Extraction Buffer (CEB), Membrane Extraction Buffer (MEB), Nuclear Extraction Buffer (NEB) and Pellet Extraction Buffer (PEB): CEB:MEB:NEB:PEB 200:200:100:100µl respectively. Fractions were stored at -80°C.

Protein concentrations of each subcellular fraction were measured using the Pierce BCA Protein Assay kit (Thermo). Samples were diluted in water (Sigma) to the lowest sample concentration to ensure the same amount of protein for each fraction was loaded into the gels. 4µl of NuPage LDS Sample Buffer (4x) were added to 16µl of each sample, which were then boiled for 10 minutes and spun down before freezing. Samples were then run as described in Western Blotting subsection.

Mass spectrometry

Preparation and TMT labelling

LM2, MDA-MB-231, and hs578t cells were reverse transfected with *DOCK5* siRNA. LM2 and MDA-MB-231 were both plated at a density of 3.3 x 10^4 cells /ml (low density, siRNA screening density) and 1.0 x 10^5 cells /ml (high density) in T75 falcons due to the requirement of 3 million cells per sample. hs578t cells were plated at 5.0 x 10^4 cells /ml. 48 hours later cells were collected by trypsinization and washed 3 x with cold PBS in clean mass spectrometry tubes. Samples were then flash frozen with 70% ethanol and dry ice. Cell pellets were dissolved in 150µL lysis buffer containing 1% sodium deoxycholate (SDC), 100mM triethylammonium bicarbonate (TEAB), 10% isopropanol, 50mM NaCl and Halt protease and phosphatase inhibitor cocktail (100X) (Thermo, #78442) on ice, assisted with pulsed probe sonication for 15 sec. Samples were subsequently boiled at 90°C for 5 min on a thermomixer and sonicated for a 5

sec additionally. Protein concentration was measured with the Coomassie Plus Bradford Protein Assay (Pierce) according to manufacturer's instructions. Aliquots containing 100µg of total protein were prepared for trypsin digestion. Samples were reduced with 5mM tris-2-carboxyethyl phosphine (TCEP) for 1h at 60 °C and alkylated with 10mM Iodoacetamide (IAA) for 30min in dark. Proteins were then digested by adding trypsin (Pierce) at final concentration 75ng/µL to each sample and incubating overnight. The resultant peptides were labelled with the TMT-10plex multiplex reagents (Thermo) according to manufacturer's instructions and were combined in equal amounts to a single tube. The combined sample was then dried with a centrifugal vacuum concentrator.

High-pH Reversed-Phase Peptide Fractionation and LC-MS/MS Analysis

Offline high pH Reversed-Phase (RP) peptide fractionation was performed with the XBridge C18 column (2.1 x 150 mm, 3.5 µm, Waters) on a Dionex Ultimate 3000 High Performance Liquid Chromatography (HPLC) system. Mobile phase A was 0.1% ammonium hydroxide and mobile phase B was 100% acetonitrile, 0.1% ammonium hydroxide. The TMT labelled peptide mixture was reconstituted in 100 µL mobile phase A and was fractionated using a gradient elution method at 0.2 mL/min with the following steps: for 5 minutes isocratic at 5% B, for 35 min gradient to 35% B, gradient to 80% B in 5 min, isocratic for 5 minutes and re-equilibration to 5% B. Fractions were collected every 42 sec and vacuum dried.

LC-MS/MS analysis was performed on the Dionex Ultimate 3000 system coupled with the Q Exactive HF Orbitrap Mass Spectrometer (Thermo Scientific). Each peptide fraction was reconstituted in 40 µL 0.1% formic acid and 7 µL were loaded to the Acclaim PepMap 100, 100 µm × 2 cm C18, 5 µm, 100 □ trapping column at 10 µL/min flow rate. The sample was then subjected to a gradient elution on the EASY-Spray C18 capillary column (75 µm × 50 cm, 2 µm) at 45 °C. Mobile phase A was 0.1% formic acid and mobile phase B was 80% acetonitrile, 0.1% formic acid. The gradient separation method at flow rate 250 nL/min was as follows: for 90 min gradient from 5%-38% B, for 10 min up to 95% B, for 5 min isocratic at 95% B, re-equilibration to 5% B in 5 min, for 10 min

isocratic at 5% B. The top 15 precursor ions between 350-1,850 m/z were selected with mass resolution of 120 k, AGC 3×10^6 and max IT 50 ms for HCD fragmentation with isolation width 1.0 Th. Collision energy was set at 35% with AGC 1×10^5 and max IT 100 ms at 60k resolution. Targeted precursors were dynamically excluded for 30 seconds.

Database search and protein quantification

The SequestHT search engine was used to analyse the acquired mass spectra in Proteome Discoverer 2.2 (Thermo Scientific) for protein identification and quantification. The precursor mass tolerance was set at 20 ppm and the fragment ion mass tolerance was set at 0.02 Da. Spectra were searched for fully tryptic peptides with a maximum of 2 miss-cleavages. TMT6plex at N-terminus/K and Carbamidomethyl at C were defined as static modifications. Dynamic modifications included oxidation of M and Deamidation of N/Q. Peptide confidence was estimated with the Percolator node. Peptide False Discovery Rate (FDR) was set at 0.01 and validation was based on q-value and decoy database search. All spectra were searched against reviewed UniProt human protein entries. The reporter ion quantifier node included a TMT 10plex quantification method with an integration window tolerance of 15 ppm and integration method based on the most confident centroid peak at the MS2 level. Only unique peptides were used for quantification, considering protein groups for peptide uniqueness. Peptides with average reporter signal-to-noise >3 were used for protein quantification.

Abundance values were scaled within each cell line and the log2 ratio of abundance in si*DOCK5* containing samples to mock transfected samples was calculated. Log2 ratios above 0.5 and below -0.5 and permutation FDR <0.05 (t-test) were considered to be proteins which were significantly up (~40% minimum increase) and down regulated (~40% minimum decrease) respectively. Statistical analysis of protemics data was done in the Perseus software[141].

Microscopy

Immunofluorescence and confocal microscopy

All performed as described for siRNA screening. Antibodies and their dilutions can be found in Tables 5 and 6. Unless otherwise stated cells were imaged using an automated Opera Quadruple Enhanced High Sensitivity (QEHS) spinning-disk confocal microscope (PerkinElmer) with 20x air lens. Lasers and their corresponding filters used were: 405(450/50), 561 (600/40), 488 (540/751), 640 (690/50).

Table 5: Primary antibodies used for Immunofluorescence (I.F) and Western Blot (W.B).

Target	Antibody and species	Company and cat number	W.B dilution	I.F Dilution
YAP/TAZ	Anti-YAP/TAZ (mouse)	Santa Cruz Biotechnologies, cat # A21235	1:1000	1:1000
α -tubulin	Anti- α-tubulin (rat)	Bio-Rad, cat # MCA77G		1:1000
GSK3β	Anti-GSK3β (rabbit)	CST, cat # 12456T	1:300	1:300
Golgi	Anti-GM180 (mouse)	Abcam, cat #52649		1:500
Beta-catenin	Anti- Beta-catenin (mouse)	BD Transduction Laboratories, cat # 610153	1:1000	1:1000
DOCK5	Anti-DOCK5 (rabbit)	Frank et al., 2017.	1:500	
PHH3	Anti- P-Histone H3 (S10) (mouse)	CST, cat # 9706S	1:1000	
KIF5B	Anti-KIF5B (rabbit)	Protein Tech, cat #231632-1-AP	1:1000	
PCNA	Anti- PCNA (mouse)	Santa Cruz Biotechnology, cat #sc-56	1:1000	

GAPDH	Anti-GAPDH (1D4) (mouse)	Novus, cat # NB300-221	1:2000	
Paxillin	Anti-Paxillin (mouse)	BD transduction labs # 610052		1:300

Table 6: Secondary antibodies used for Immunofluorescence (I.F) and Western Blot (W.B).

Secondary antibody/dyes	Company	Dilution
Phalloidin	Invitrogen, cat # A12379	1:1000
Hoechst	Sigma Aldrich, cat # 33258	1:1000
AlexaFluor 647 goat anti-mouse	Life Technologies, cat # A21235	1:1000
AlexaFluor 568 goat anti-rat	Life Technologies, cat # A11077	1:1000
AlexaFluor 647 goat anti-rabbit	Life Technologies, cat # A21245	1:1000
AlexaFluor 568 goat anti-rabbit	Life Technologies, cat # A11036	1:1000
Anti-mouse IgG, HRP-linked antibody	CST, cat #7076S	1:2000
Anti-rabbit IgG, HRP-	CST, cat #7074S	1:2000

linked antibody		

Focal adhesion dynamics and Total Internal Reflection Fluorescence Imaging (TIRF)

LM2 CAAX-GFP cells were transfected with either just Talin mApple plasmid or both Talin mApple and si*DOCK5,* si*RAC,* si*RHOA*, or si*CDC42* as stated in the transfections section. 35mm glass Mat-tek dishes were coated with 10µg/ml Fibronectin (human plasma, Sigma #F0895) for 1 hour. Fibronectin was then aspirated and Mat-tek dishes were washed 3 x PBS and left to dry. 48 hours after transfection, LM2 CAAX-GFP cells were plated at 1.5 x 10^5 cells /ml in 1ml of Liebnevitz medium (10% FBS, 1% penicillin/streptomyocin). Cells were live imaged using the TIRF (3i) approximately 1 hour after seeding. Lasers used were 647 And 488. Images were taken either every 3 minutes or every 1.5 minutes. Images were acquired using Slidebook software (3i). Videos were processed to be the same length and analysed using the 'Focal Adhesion Analysis Server (FAAS)' (Berginski and Gomez, 2013). Videos containing the same number of time frames were compared.

We displayed the data using estimation statistics using a website generated by Ho et al., 2019, as we think that by showing the effect size we can visualise and understand this type of data better.

Spreading assay and Super-Resolution via Optical-Reassignment (SoRa) microscopy

Cells pertaining to experiments imaged using the SoRa were fixed and stained with a slight variation to those from RNAi screens. Briefly, cells were reverse transfected as described in the transfection section in 6 well plates, and plated on 35mm glass Mat-tek dishes coated with 10µg/ml Fibronectin as described for TIRF, at a density of 1.5 x 10^5 cells /ml 48 hours after transfection. They were fixed 3 hours after plating with paraformaldehyde in PBS (4% final concentration), permeabilised with 0.1% Triton-X-100 in PBS for 10 minutes, and blocked with 0.5% BSA dissolved in PBS with 0.3ml of glycine for 1 hour.

Antibody incubations were performed in 0.5% BSA. Primary antibodies were added at RT for 1.5 hours. Secondary antibodies were added for 1.5 hours at RT. Hoechst was used as a DNA stain and left for 15 minutes at the end at RT. Cells were washed 3 x with PBS between each step and were left in 200µl of PBS. Where antibodies used were close in species such as mouse and rat, they were added sequentially to avoid any possible bleedthrough. Antibodies and their dilutions can be found in Tables 5 and 6. When drugs were used, they were added in 500µl on top of the 2ml solution of cells immediately after plating, with final concentrations as shown in Table 2. Cells were imaged using the SoRa (3i) microscope.

Wound heal assay

Cells were reverse transfected as previously described and were plated in a 96 well Perkin Elmer Cell Carrier Ultra plate at a density of 2.7 x 10^6 cells/ml. 48 hours later a 10µM pipette tip was used to scratch the monolayers from top to bottom of the well, resulting in a vertical cell-free gap or wound. Medium was removed and wells were carefully washed with warm PBS so as to remove debris. 100µL of fresh medium was them added to all wells. Imaging began as soon as the wound was created, using a Basic Confocal Spinning Disk Microscope (3i). Images were taken every 10 minutes for 16 hours. Images were processed using ImageJ. We quantified Golgi orientation in cells that had their Golgi within 180 degrees of the wound and quantified the angle of orientation by drawing a line from the position of the Golgi towards the wound and another parallel to the wound (Fig. 7e, ii) as in Zhang et al., 2008[110]. A 90 degree angle is indicative of Golgi facing toward the wound and indicative of front-rear polarity.

Growth curve assay

Cells were reverse transfected in 6-well plates and plated at a density of 3.3 x 10^4 cells/ml per well, with three replicates per condition. When drugs were used one plate containing mock transfected cells and *DOCK5* siRNA would be treated with DMSO, and another with the drug. Binimetinib (MEKi) and FAKi

(PF-573288) were added to a final concentration of 10µM and 2µM respectively. Drugs and DMSO were added in 500µl DMEM 48 hours after transfection. Plates were incubated in the IncuCyte S3 Live-Cell Analysis System (Sartorius) at 37°C and 5% CO_2 and imaged at 6 hour time points for a minimum of 156 hours (6.5 days). A minimum of 9 fields of view were imaged per well. Analysis of confluence over time was carried out using IncuCyte software (Sartorius). To compare confluence between conditions at a point where mock transfected cells reached 50% or 100% confluency, each well was normalized to the mock transfected wells for each plate, prior to statistical analysis. Representative growth curves are shown per plate with the average of three wells per condition.

Statistical analyses

Statistical analyses performed for each assay are indicated in text and figure legends. Most analyses were carried out using Prism 8 (GraphPad). PCA analysis was performed in Jupyter Notebooks[143]. Hierarchical clustering and heat maps were made with Morpheus Broad Institute Software[144].

.

Acknowledgements

We thank Nicola Ferrari (Astex Pharmaceuticals, UK) for the CAAX-GFP construct, Aaron Farrugia for 2-photon imaging (ICR, London, UK), and Vicky Bousgouni (Dynamical Cell Systems Team, ICR, London, UK) for assistance with the RNAi library array and helpful comments on the manuscript. We thank Oliver Rocks (Max-Delbrück-Center for Molecular Medicine, Berlin, Germany) for the DOCK5-YFP construct and Steen Hansen (Boston Children's Hospital, Boston, USA) for the DOCK5 antibody. We thank Frankie Butera for helpful comments on the manuscript. This work was funded by a Cancer Research UK and Stand Up to Cancer UK Programme Foundation Award to C.B. (C37275/1A20146). The work of T.I.R and J.S.C was funded by the CRUK Centre grant with reference number C309/A25144.

Author Contributions

P.P.-V. contributed to experimental design, carried out the experiments, performed image and data analysis, wrote and prepared the manuscript. M.A.-G. optimized RNAi screening methodology, performed experiments, data and image analysis. T.I.R, J.S.C performed mass spectrometry and proteomic analysis. C.B contributed to experimental design, imaging, and manuscript preparation.

Competing interests

The authors declare no competing interests.

Figure legends

Figure 1. DOCK5 regulates YAP/TAZ localisation.

(a) Graph depicting Z-scores of log YAP/TAZ ratios following knockdown of Rho GTPases. si*LATS1/2* included as controls for YAP/TAZ translocation. mean ± s.d (n = 3-4 wells per condition, 1000 cells per well, one-way ANOVA to mock). (b) Z-scores per well for YAP/TAZ ratio for OTP siRNA screen in LM2. Above 1.5 (red dotted line) are siRNAs which are hits for high YAP/TAZ ratio and thus can be considered inhibitors of YAP/TAZ. Below -1.5 (red dotted line) are siRNAs which are hits for low YAP/TAZ ratio and thus can be considered YAP/TAZ activators. *LATS1/2* and *YAP* siRNAs included as controls for high and low YAP/TAZ ratios are shown. Four individual replicates for si*DOCK5* are shown. (c) Representative images showing YAP/TAZ staining for mock transfected and si*DOCK5* transfected LM2 cells. Arrows point to cells with high YAP/TAZ ratio (mock) and low YAP/TAZ ratio (si*DOCK5*). Graphs showing

quantification of YAP/TAZ ratio, and whole cell YAP/TAZ levels in mock versus si*DOCK5.* si*YAP* + si*TAZ* show YAP/TAZ antibody is working appropriately. mean ± s.d (n = 3 independent biological repeats separate from screen data, dots represent individual wells, Student's t-test (left) and ANOVA (right). d) qRTPCR showing *DOCK5* mRNA levels in mock versus si*DOCK5* transfected cells. mean ± s.d (n = 3 biological repeats, at least 3 technical replicates each, Student's t-test). (e) Validation of si*DOCK5* resulting in a decrease in YAP/TAZ ratio via subcellular fractionation. (i) Representative western blot of subcellular fractions for mock and si*DOCK5*. Nuc: nuclear fraction. Mem: membrane fraction. Cyt: cytoplasm fraction. Blotted for DOCK5, YAP and TAZ. Same amounts of protein loaded (6.5ng). (ii) Quantification of ratio of YAP/TAZ in the nucleus to the cytoplasm fraction from western blots of subcellular fractionations. mean ± s.d (n = 2). Student's t-test. (iii) Representative distribution of YAP/TAZ in all fractions with and without *DOCK5*. (f) (i) Immunofluorescence images and (ii) quantification of YAP/TAZ localisation in mock or si*DOCK5* transfected cells treated with DMSO or DOCK5 inhibitor C21. mean ± s.d (n = 9 wells/condition, 1000 cells/well, one-way ANOVA). Significance for all panels: * P < 0.05, ** P < 0.001 *** P < 0.001, **** P < 0.0001.

Figure 2. DOCK5 contributes to growth and drug resistance in LM2 cells

(a) Fold change to control mock transfected wells at 50% confluency for growth curves (Figure 2b-d and Supplementary Figure 2). Each data point is from one well. mean ± s.d, Student's t-test. (b-d) Growth curves for (b) si*DOCK5*, si*CDC42*, si*DOCK5* + si*CDC42*, (c) si*DOCK5*, si*RAC1*, si*DOCK5* + si*RAC1,* (d) si*DOCK5*, si*RHOA*, si*DOCK5* + si*RHOA* transfected cells. Averages per well are shown. (e) (g) (h) Growth curves and (i) representative images at 50% confluency for mock and si*DOCK5* transfected cells treated with DMSO (closed circle, square) and 10 µM final MEKi Binimetinib (open circle, square) for (e) MDA-MB-231, (g) A375P, (h) LM2. (f, j) Fold change to control mock transfected wells at 100% and 50% confluency respectively for LM2, MDA-MB-231, and A375 mock and si*DOCK5* transfected cells treated with DMSO or Binimetinib. Each data point is from one well. mean ± s.d. Scale bar is 400 µm. All experiments performed in triplicate, representative experiment shown with n

= 3 wells per condition. One-way ANOVA. For all panels: * P < 0.05, ** P < 0.01, *** P < 0.001, **** P < 0.0001.

Figure 3 Shape classification and relationship with YAP/TAZ.

(a) Heat map and dendrogram of the features describing each shape and which Columbus software used to classify cells into the five visually distinctive reference shapes, as well as their contribution, using single cell data. Yellow and blue represent a high and low score respectively in arbitrary units. (b) Images from one field of view from mock transfected well with cells coloured by their classified shape by software showing highly heterogenous population, and (c) the percentage of cells classified into each shape in one sample mock transfected well and (d) for an siRNAs which was a top hits for spindly shape, depicting a rearrangement in the shapes seen for mock-transfected cells. (e) Graph depicting Z-score of log10 ratio of nuclear to ring region YAP/TAZ for single LM2 cells following transfection with siRNA which results in the biggest enrichment for each particular shape: si*ECT2* for large, si*DOCK11* for fan, si*ARHGAP5* for small round, si*DOCK10* for triangular, si*FAM13A* for spindly. Mean ± sd are shown. Data taken from at least 5 fields of view from 2 wells. (f) Images of population from which single cell data shown in (e) were taken. Arrows indicate examples of nuclear YAP/TAZ for each shape. Images stained for YAP/TAZ (red) and F-actin (green). Scale bar is 50µm.

Figure 4. DOCK5 regulates shape.

(a) (i) Clustering of high-dimensional quantitative signatures based on the effect of RhoGEF/GAPs and Rho GTPase siRNAs on the TNBC cell line LM2. Columns are Z-score values of the percentage of cells classified into that shape when said siRNA is depleted. Red and blue indicate high and low values respectively. Clustering performed using Pearson correlation. 11 clusters were identified and defined as genes grouped at the highest node of clustering with a value of uncentered Pearson correlation coefficient above 0.73. Numbering indicates clusters and images are representative for mock and siRNAs which enrich for a particular shape in example clusters. Staining shows DNA (blue), tubulin (yellow), F-actin (green) and YAP/TAZ (red). Scale bar is 50 µm. (b)

Clustering of QMS for siRNAs shown as well as C21 treatment at a Pearson correlation of 0.74. Images for si*RAC2*, C21, si*LATS1*, and si*YAP* are shown, stained for DNA (blue), tubulin (yellow), F-actin (green) and YAP/TAZ (red). Scale bar is 50 µm.

Figure 5. DOCK5 depletion reduces single cell invasion in 3D collagen assays and Matrigel spheroid assays

(a) Representative 2-photon images of LM2 cells (GFP) stained for DNA (blue) mixed with rat-tail collagen I at 2 mg/ml (white) at the bottom of the plate (0 µm plane) and the middle (30 µm plane). (b) Representative confocal spinning disk images (12 fields per well) for knockdowns shown in (c) at 0 µm and 30 µm. (c) Graph shows quantification of invasion index for knockdowns in rat-tail collagen I at 2 mg/ml. Invasion index is indicative of the number of cells in middle planes divided by total number of cells in all planes quantified, including bottom plane. Mean ± sd (n > 3 wells per condition, 1000 cells/well. ANOVA, **** P < 0.0001). (d) Invasion index of mock versus si*DOCK5* transfected cells at collagen concentrations: 1.6mg/ml, 3.8mg/ml, and 4.8mg/ml. Mean ± sd (n > 3 wells per condition, 1000 cells/well, ANOVA, ** P < 0.01). Scale bars, 100 µm. (e) Representative images of mock transfected cells and si*DOCK5* transfected cell spheroids 48 hours post transfection and pre 100% Matrigel (left), and one (middle) and six (right) days post 100% Matrigel addition. Scale bar is 200µm. (f) Graphs show quantification of area of Matrigel invaded (top) and proliferation area (bottom) in arbitrary units over 8 days post adding 100% Matrigel to the spheroids. Proliferation area refers to how much the spheroid increased in size without invading into the matrix. Mock transfected cells in black, si*DOCK5* transfected cells in red. Each line represents one well. n > 3 wells. Statistical significance obtained by performing student t-test on row means (* P = 0.0294, ** P < 0.01).

Figure 6. Proteomic data indicative of polarity and cell cycle defects with si*DOCK5*. (a) Heat map of proteins significantly up or downregulated following *DOCK5* knockdown via siRNA in TNBC cell lines. Significance based on Log2 ratios for protein levels of si*DOCK5* v mock being above 0.5 and below -0.5 and permutation FDR <0.05 (t-test). 1 to 5 are mock transfected, while 6 to 10 are

transfected with si*DOCK5*. 1 and 6: LM2 plated at low (screen) density; 2 and 8: LM2 plated at high density; 3 and 7: MDA-MB-231 plated at low (screen) density; 4 and 9: MDA-MB-231 plated at high density; 2 and 4: LM2 plated at high density; 5 and 10: hs578t. Red and blue indicate high and low protein abundance levels (row max to min respectively). Proteins up and downregulated based on Log2 value. Proteins involved in regulating polarity and AKT signaling pathways shown are shown as well as CTGF. YAP/TAZ targets shown in bold (b) Top protein abundance levels of Rho GTPases and DOCK1 that were unchanged with si*DOCK5* abundance levels for comparison. Bottom protein levels of Rho GTPases and RhoGEF/GAPs which were significantly upregulated or downregulated upon DOCK5 knockdown. Row max (red) to min (blue). (c) Top: Heat map of protein levels of proteins regulating polarity that were significantly up and down regulated. Values normalized to cell line. Row max (red) to min (blue). Bottom: abundance levels of proteins of interest that were not significantly up or downregulated, with si*DOCK5* abundance levels for comparison. (d) (i) Representative images and (ii) immunofluorescence quantification of GSK3β at the membrane in mock and si*DOCK5* transfected cells in DMSO or DOCK5 inhibitor C21 Mean per well ± sd (n > 3 wells/condition, 1000 cells/well; ANOVA). White arrows indicate GSK3β at the membrane (mock) and lack thereof (si*DOCK5* and C21). GSK3β imaged at 40x, Scale bar, 20 µm. (e) (f) Immunofluorescence quantifications of (e) pGSK3β membrane levels and (f) YAP/TAZ ratio of mock and si*DOCK5* transfected cells treated with DMSO (black), 5mM LiCl (pink) or 2µM final Uprosertib (green). Mean per well ± sd are shown (n > 3, 1000 cells/well, 2 ways ANOVA, Tukey's multiple comparison's test * $P < 0.05$, ** $P < 0.01$, *** $P < 0.001$, **** $P < 0.0001$). (g) Immunofluorescence images of YAP/TAZ for mock and si*DOCK5* transfected cells treated with DMSO (black), 5mM LiCl (pink) or 2µM final Uprosertib quantified in (f). Scale bar, 50 µm.

Figure 7. DOCK5 depletion reduces wound closure migration rates and affects Golgi orientation

(a) Brightfield images at 0, 10 and 16 hours post creating scratch wound for mock, si*DOCK5*, si*YAP*, si*TAZ*, and si*YAP* + si*TAZ* transfected cells. Dotted

black line indicates the starting line from where cells migrated over time. Scale bar, 100 µm. (b) Graph shows migration rates (µm/hour) (n = 5 wells per condition, with at least 2 biological repeats). Values were normalised to average of mock for each biological repeat. Mean ± sd, one-way ANOVA to mock. *** P < 0.001, **** P < 0.0001 (c), (d) Percentage frequency of cells with Golgis orientated 0, 30, 60, 90, 120, 150, and 180 degrees relative to the wound depicted as a bar chart (c) and as a windrose plot (di,ii). Percentages indicated on windrose plots. (e) Images depicting Golgi immunofluorescence stain and Hoechst, wound is shown with white dotted line. Angle measuring relative to wound is depicted in (ii), example of 90 degree angle and orientation towards the wound. Scale bar is 50 µm.

Figure 8. DOCK5 depletion alters focal adhesion dynamics

(a) Overexpressed DOCK5-tagged YFP localises to focal adhesions (paxillin). Cells stained for paxillin (red), tubulin (blue). Scale bar is 5 µm. (b) Sequences of zoomed in sections of mock, and si*DOCK5* transfected LM2-CAAXGFP cells over time. Frames are every 3 minutes. Arrows indicate an example of an adhesion to follow. Dotted line represents the edge of the cell at the beginning of each sequence of frames shown. Adhesion signal represents Talin mApple intensity: red more intense, blue less intense. Scale bar is 2 µm. (c) (i) Representative images of how Focal Adhesion Analysis Server (FAAS)[145] picks up adhesions on mock and si*DOCK5* transfected cells. Scale bar is 10 µm. (ii) Focal adhesions tracked over time in same cells as in (i). Blue to red indicates adhesions which have been present for less, and longer amounts of time respectively. (d) (e) Cumming estimation plots of Hedge's g for comparison between (d) assembly and disassembly rates, and (e) assembly phase length and disassembly phase length of adhesions in mock versus si*DOCK5* transfected cells. N shows number of adhesions quantified, data from 4 cells. Raw data is plotted in the top axes, while mean difference is plotted in lower axes as a bootstrap sampling distribution. Mean differences are shown as dots, 95% confidence intervals are shown by the ends of the vertical error bars. Generated using Ho et al., 2019[142] website. (d) Unpaired Hedge's g between mock and si*DOCK5* for assembly and disassembly rates are 1.65 (95% CI 1.33, 1.96), and 1.28 (95% CI 1.07, 1.50) respectively. Two-sided P values of Mann-

Whitney tests are 3.64 x 10^{-15}, and 1.04 x 10^{-15} for assembly and disassembly rates respectively. (e) Unpaired Hedge's g between mock and si*DOCK5* for assembly phase length and disassembly phase length are 0.101 (95% CI -0.199, 0.405), and -0.00986 (95% CI -0.38, 0.155) respectively. Two-sided P values of Mann-Whitney tests are 0.602, and 0.437 for assembly and disassembly phase lengths respectively. N number is individual adhesions from 4 cells, filtered by them being present for a minimum of 5 frames (phase length 5) and mean axial ratio less than 3. Unpaired Mann-Whitney test, $P < 0.001$.

Figure 9. CDC42 and RHOA depletion affect FA morphogenesis in metastatic cells

(a) Representative images of LM2-CAAXGFP cells transfected with Talin mApple and si*DOCK5*, si*CDC42*, si*RHOA*, si*RAC1*, mock, and treated with the AKT inhibitor Uprosertib. Left and right panels per condition show FAAS picking up the adhesions and adhesions tracked over time for the same cell. (b) (c) (d) Cumming estimation plots of Hedge's g for comparison between (b) assembly and (c) disassembly rates, as well as (d) stability phase length of adhesions in mock versus si*DOCK5,* si*CDC42*, si*RHOA*, si*RAC1* transfected cells, and Uprosertib treated cells. n shows number of adhesions. Data is taken from 3 cells per condition. Raw data is plotted in the upper axes, while mean difference is plotted in lower axes as a bootstrap sampling distribution. Mean differences are shown as dots, 95% confidence intervals are shown by the ends of the vertical error bars. Generated using Ho et al., 2019[142] website. (b) Unpaired Hedge's g for assembly rates between mock and conditions: si*DOCK5*: 0.375 (95% CI -0.0214, 0.776); si*CDC42*: 0.851 (95% CI -0.499, 1.19); si*RHOA*: 1.06 (95% CI -0.229, 0.436); si*RAC1*: 0.0311 (95% CI -0.332, 0.387); Uprosertib: 0.105 (95% CI -0.276, 0.479). Two-sided P values of Mann-Whitney tests are 0.242, 2.090 x 10^{-5}, 0.922, 0.963, 0.808 respectively. (c) Unpaired Hedge's g for disassembly rates between mock and conditions: si*DOCK5*: 0.574 (95% CI 0.0979, 1.04); si*CDC42*: 0.321 (95% CI -0.0767, 0.715); si*RHOA*: 0.376 (95% CI 0.0138, 0.732); si*RAC1*: 0.145 (95% CI -0.252, 0.558); Uprosertib: 0.467 (95% CI 0.0641, 0.887). Two-sided P values of Mann-Whitney tests are 0.0363, 0.1840, 0.0580, 0.4030, 0.0652 respectively. (d) Unpaired Hedge's g for

stability phase lengths between mock and conditions: si*DOCK5*: -0.507 (95% CI -1.20, 0.494); si*CDC42*: 0.167 (95% CI -0.464, 0.856); si*RHOA*: -0.395 (95% CI -1.03, 0.517); si*RAC1*: -0.299 (95% CI -0.827, 0.259); Uprosertib: -0.456 (95% CI -1.04, 0.393). Two-sided P values of Mann-Whitney tests are 0.0602, 0.6390, 0.06080, 0.4590, 0.0476 respectively. (e) Histogram of assembly phase lengths for all conditions (top) and unpaired Hedge's g for assembly rate phase lengths between mock and conditions (bottom): si*DOCK5*: 0.307 (95% CI -0.0508, 0.662); si*CDC42*: 0.256 (95% CI -0.0605, 0.536); si*RHOA*: -0.0537 (95% CI -0.35, 0.247); si*RAC1*: 0.336 (95% CI 0.0297, 0.621); Uprosertib: -0.187 (95% CI -0.471, 0.148). Two-sided P values of Mann-Whitney tests are 0.140, 0.154, 0.471, 0.237, 0.390 respectively. Mock n = 83, si*DOCK5* n = 56, si*CDC42* n = 74, si*RHOA* n = 83, si*RAC1* n = 67, Uprosertib n = 61. (f) Histograms of disassembly phase lengths (top) and unpaired Hedge's g for disassembly rate phase lengths between mock and conditions (bottom): si*DOCK5*: -0.12 (95% CI -0.439, 0.39); si*CDC42*: 0.106 (95% CI -0.224, 0.483); si*RHOA*: -0.255 (95% CI -0.505, 0.0726); si*RAC1*: -0.251 (95% CI -0.494, 0.14); Uprosertib: 0.037 (95% CI -0.285, 0.456). Two-sided P values of Mann-Whitney tests are 0.550, 0.633, 0.270, 0.435, 0.818 respectively. Mock n = 92, si*DOCK5* n = 35, si*CDC42* n = 50, si*RHOA* n = 64, si*RAC1* n = 42, Uprosertib n = 50. (g) Summary of results and how each siRNA and treatment is affecting adhesion life cycle. Not to scale.

Figure 10. DOCK5 and CDC42 stabilise polarity. Images taken on SoRA for mock, si*DOCK5*, si*CDC42,* si*RAC1*+ si*RAC2,* si*RHOA,* and treated with FAKi, and Blebbistatin. Stained for DNA (blue), Paxillin (orange), α-tubulin (pink), F-actin (green). Merge 2D and 3D projections. Scale bar = 10µm.

Figure 11 DOCK5 promotes spreading following MT depolymerisation

(a) Immunofluorescence images of mock or si*DOCK5* transfected cells treated just with DMSO, or treated with nocodazole (NZ) for 4 hours and then washed out in either media containing DMSO, NZ, or taxol (TX). Stained for DNA (blue), tubulin (yellow), and F-actin (green). Scale bar is 50 µm. Zoomed in images from 384 well plate taken and shown with same intensity settings. (b-d) Quantifications of (a) showing (b) cell area, (c) whole cell SER Ridge tubulin (texture), and (d) actin intensity at the membrane. Mean per well ± sd are

shown (n > 3 wells, 1000 cells/well, 2 ways ANOVA, Tukey's multiple comparison's test * P < 0.05, ** P < 0.01, *** P < 0.001, **** P < 0.0001). Significance between Mock and si*DOCK5* for each condition shown with no bars. Significance between mock NZ (black) and si*DOCK5* NZ (red) compared to other treatments for same transfection.

Figure 12 DOCK5 acts at FAs in breast cancer cells to establish positive feedback loops which maintain polarity in the presence of stable integrin-ECM attachments and cellular tension.

Schematic of proposed model where in WT conditions DOCK5 gets recruited to FAs and acts as GEF for RAC-type GTPase to promote FA assembly and turnover/maturation in a positive feedback loop. At the same time DOCK5 recruits and activates AKT to FAs near the leading edge stabilising GSK3β, which is targeted by CDC42-PKCζ for phosphorylation, leading to the maintenance of polarity. Here DOCK5 increases the levels of AKT and thus promotes further GSK3β stability and phosphorylation in another positive feedback loop. Further, actomyosin engagement by FA results in high RHOA and consequently high nuclear YAP/TAZ. Finally, DOCK5 could potentially mature FAs to recruit CDC42 GEFs which can further amplify CDC42 activation at the leading edge.

Supplementary Figure 1. Validation of *DOCK5* siRNA knockdown. (a) Graph depicting log10 ratio of nuclear to ring region YAP/TAZ versus cell number for MDA-MB-231 (light blue), LM2 (dark blue), SUM159 (orange), hs578t (yellow), T47D (pink), and MCF10A (orange). Representative images of hs578t, SUM159, MCF10A, T47D, MDA-MB-231, and LM2 at low (3.3×10^4 cells/ml) and high (1.3×10^5 cells/ml) densities, stained for YAP/TAZ. As well as 2.7×10^5 cells/ml for MCF10A and T47D. n = 4 wells/condition. Scale bar is 50µm. (b) Z-scores per well for YAP/TAZ ratio for siGENOME siRNA screen in LM2. Above 1.5 (red dotted line) are siRNAs which are hits for high YAP/TAZ ratio (YAP/TAZ inhibitors). Below -1.5 (red dotted line) are siRNAs which are hits for low YAP/TAZ ratio (YAP/TAZ activators). Four individual replicates for si*DOCK5* as hits for low YAP/TAZ ratio are shown. (c) Validation of DOCK5 siRNA knockdown via qRTPCR. *DOCK5* mRNA levels following *DOCK5*

knockdown with deconvoluted siRNAs for DOCK5 OTP5 to 8 and in pooled combination (OTP pool), as well as siG1-4 and in pooled combination (siGENOME pool). Mean ± sd (n = 4 wells, ANOVA, **** P < 0.0001). (d) Graphs showing YAP/TAZ ratio and YAP/TAZ levels upon transfection with DOCK5 deconvoluted and pooled siRNAs for OTP and siGENOME. Mean ± sd (n > 3 wells, 1000 cells/well. ANOVA, *P < 0.1** P < 0.01, *** P < 0.001**** P < 0.0001). (e) Representative western blot of subcellular fractions for mock and si*DOCK5*. 1: nuclear fraction; 2: membrane fraction; 3: cytoplasm fraction; 4: chromatin bound fraction, 5: cytoskeletal fraction. M is mock, D5: si*DOCK5*. Blotted for YAP and TAZ. Loaded 5ng of protein for all except for cytoskeleton (2.5ng). Below, quantification of DOCK5 protein levels upon *DOCK5* knockdown adding all fractions from western blot. Mean ± sd (n = 2, Student's t-test, **** P < 0.0001). (f) Same subcellular fractions as in (e) blotted for PH3B, KIF5B, GAPDH, and PCNA as controls for each fraction: chromatin bound, cytoskeleton bound, whole cell, nuclear respectively. Pie charts depicting the distribution of (i) PCNA, (ii) KIF5B, (iii) PH3B, in each fraction.

Supplementary Figure 2. RHOA, RAC1, YAP, TAZ depletion do not affect growth rates. Growth curves for mock and (a) si*DOCK5*, (b) si*CDC42* (c) si*RHOA*, (d) si*RAC1*, (e) si*YAP* (f) si*TAZ* and (g) si*YAP* + si*TAZ* transfected cells. Mock and siRNA transfected wells represented as circles and squares respectively. Experiments performed in triplicate, representative experiment shown with n = 3 wells per condition. Averages per well are shown.

Supplementary Figure 3. Shape filtering in LM2

(a) (b) PCA of single cell dataset comprised of texture and morphological features of populations which were either mock transfected (a) or transfected with siRNAs which scored the highest for enriching for a particular shape (b). Each data point represents a cell and is colour coded by the shape into which it has been classified. Spindly in red, round large in green, triangular in blue, fan in black, and small round in purple. Black box represents 1 standard deviation of the mean for PC1 and PC2 of (b), projected on (a). Single cells within black

box shown in (a) were defined as ‘normal’ in the new classifiers. (c) PCA of single cell dataset comprised of texture and morphological features of siRNA transfected population, after running new classifiers on same data, removing cells classified as ‘normal’. Ellipses represent 95% confidence intervals for each shape.

Supplementary Figure 4. Beta catenin upregulation in response to LiCl treatment and increased nuclear FOXO3A upon Uprosertib treatment (a) (a) Representative images of mock transfected cells treated with DMSO, 5mM LiCl, or 2μM final Uprosertib. Stained for FOXO3A (yellow), YAP/TAZ (red), and merge including F-actin (green) and DNA (blue). Scale bar is 50 μm. Arrows point to nuclear FOXO3A and YAP/TAZ which are higher and lower respectively in Uprosertib. (b) Quantification of FOXO3A nuclear to cytoplasmic ratio (log) shown in a. Mean ± sd are shown (n > 3 wells, 1000 cells per well. ANOVA, **** P < 0.0001). (c) Representative images of mock transfected cells treated with DMSO, 5mM LiCl, 2μM final Uprosertib. Stained for GSK3β (yellow), βcatenin (red), and merge including F-actin (green) and DNA (blue). Scale bar is 50 μm. Arrows indicate GSK3β at leading edge and increased beta catenin. (d) Quantification of beta catenin shown in b. Mean ± sd are shown (n > 3 wells, 1000 cells per well. ANOVA, **** P < 0.0001).

Supplementary Figure 5. Automated segmentation for Collagen Invasion Quantification. Images for mock and si*DOCK5* transfected cells shown at planes quantified: bottom plane 0μm and middle plane 30μm. As well as intermediate planes 15μm, and 45μm. Cells selected indicate cells that the software has identified to be in that particular plane (green) following a filtering process. Those that are not considered to be in that plane are in red. Shows that cells which are counted in middle plane are not spanning other planes. Scale bar is 50 μm.

Supplementary Video 1. Video showing LM2-CAAX GFP cell overexpressing Talin mApple (white). Total video time is 63 frames with each frame taken every 3 minutes. Exported at 7 frames per second.

Supplementary Video 2. Video showing LM2-CAAX GFP cell transfected with si*DOCK5* and overexpressing Talin mApple (white). Total video time is 63 frames with each frame taken every 3 minutes. Exported at 7 frames per second.

References

1. Etienne-Manneville, S. Polarity proteins in migration and invasion. *Oncogene* **27**, 6970–6980 (2008).
2. Ridley, A. J. *et al.* Cell Migration: Integrating Signals from Front to Back. *Science* **302**, 1704–1709 (2003).
3. Etienne-Manneville, S. Cdc42 - the centre of polarity. *J. Cell Sci.* **117**, 1291–1300 (2004).
4. Etienne-Manneville, S. & Hall, A. Cell polarity: Par6, aPKC and cytoskeletal crosstalk. *Curr. Opin. Cell Biol.* **15**, 67–72 (2003).
5. Hall, A. Rho GTPases and the Actin Cytoskeleton. *Science* **279**, 509–514 (1998).
6. Ridley, A. J. Rho GTPases and cell migration. *J. Cell Sci.* **114**, 2713–2722 (2001).
7. Gardel, M. L., Schneider, I. C., Aratyn-Schaus, Yvonne & Waterman, C. M. Mechanical Integration of Actin and Adhesion Dynamics in Cell Migration. *Annu. Rev. Cell Dev. Biol.* **26**, 315–333 (2010).
8. Pertz, O., Hodgson, L., Klemke, R. L. & Hahn, K. M. Spatiotemporal dynamics of RhoA activity in migrating cells. *Nature* **440**, 1069–1072 (2006).
9. Ridley, A. J. Historical Overview of Rho GTPases. in *Rho GTPases* (ed. Rivero, F.) vol. 827 3–12 (Springer New York, 2012).
10. Clark, E. A., Golub, T. R., Lander, E. S. & Hynes, R. O. Genomic analysis of metastasis reveals an essential role for RhoC. *Nature* **406**, 532–535 (2000).
11. Fife, C. M., McCarroll, J. A. & Kavallaris, M. Movers and shakers: cell cytoskeleton in cancer metastasis: Cytoskeleton and cancer metastasis. *Br. J. Pharmacol.* **171**, 5507–5523 (2014).
12. Jansen, S., Gosens, R., Wieland, T. & Schmidt, M. Paving the Rho in cancer metastasis: Rho GTPases and beyond. *Pharmacol. Ther.* **183**, 1–21 (2018).
13. Lawson, C. D. & Ridley, A. J. Rho GTPase signaling complexes in cell migration and invasion. *J. Cell Biol.* **217**, 447–457 (2018).
14. Sahai, E. & Marshall, C. J. RHO–GTPases and cancer. *Nat. Rev. Cancer* **2**, 133–142 (2002).

15. Bos, J. L., Rehmann, H. & Wittinghofer, A. GEFs and GAPs: Critical Elements in the Control of Small G Proteins. *Cell* **129**, 865–877 (2007).
16. Jaffe, A. B. & Hall, A. RHO GTPASES: Biochemistry and Biology. *Annu. Rev. Cell Dev. Biol.* **21**, 247–269 (2005).
17. Müller, P. M. *et al.* Systems analysis of RhoGEF and RhoGAP regulatory proteins reveals spatially organized RAC1 signalling from integrin adhesions | Nature Cell Biology. https://www.nature.com/articles/s41556-020-0488-x?proof=true (2020).
18. Jaffe, A. B. & Hall, A. Rho GTPases in transformation and metastasis. in *Advances in Cancer Research* vol. 84 57–80 (Academic Press, 2002).
19. Rossman, K. L., Der, C. J. & Sondek, J. GEF means go: turning on RHO GTPases with guanine nucleotide-exchange factors. *Nat. Rev. Mol. Cell Biol.* **6**, 167–180 (2005).
20. Fort, P. & Blangy, A. The Evolutionary Landscape of Dbl-Like RhoGEF Families: Adapting Eukaryotic Cells to Environmental Signals. *Genome Biol. Evol.* **9**, 1471–1486 (2017).
21. Adamowicz, M. *et al.* Frequent amplifications and abundant expression of TRIO, NKD2, and IRX2 in soft tissue sarcomas. *Genes. Chromosomes Cancer* **45**, 829–838 (2006).
22. Cook, D. R., Rossman, K. L. & Der, C. J. Rho guanine nucleotide exchange factors: regulators of Rho GTPase activity in development and disease. *Oncogene* **33**, 4021–4035 (2014).
23. Gatza, M. L., Silva, G. O., Parker, J. S., Fan, C. & Perou, C. M. An integrated genomics approach identifies drivers of proliferation in luminal-subtype human breast cancer. *Nat Genet* **46**, 1051–1059 (2014).
24. Lane, J., Martin, T. A., Mansel, R. E. & Jiang, W. G. The expression and prognostic value of the guanine nucleotide exchange factors (GEFs) Trio, Vav1 and TIAM-1 in human breast cancer. *Int. Semin. Surg. Oncol.* **5**, 23 (2008).
25. Laurin, M. *et al.* Rac-specific guanine nucleotide exchange factor DOCK1 is a critical regulator of HER2-mediated breast cancer metastasis. *Proc. Natl. Acad. Sci.* **110**, 7434–7439 (2013).
26. Sosa, M. S. *et al.* Identification of the Rac-GEF P-Rex1 as an essential mediator of ErbB signaling in breast cancer. *Mol. Cell* **40**, 877–892 (2010).
27. Shriver, M. *et al.* Loss of giant obscurins from breast epithelium promotes epithelial-to-mesenchymal transition, tumorigenicity and metastasis. *Oncogene* **34**, 4248–4259 (2015).
28. Sjöblom, T. *et al.* The consensus coding sequences of human breast and colorectal cancers. *Science* **314**, 268–274 (2006).
29. Bravo-Cordero, J. J. *et al.* A Novel Spatiotemporal RhoC Activation Pathway Locally Regulates Cofilin Activity at Invadopodia. *Curr. Biol.* **21**, 635–644 (2011).
30. Liu, Z., Adams, H. C. & Whitehead, I. P. The Rho-specific Guanine Nucleotide Exchange Factor Dbs Regulates Breast Cancer Cell Migration. *J. Biol. Chem.* **284**, 15771–15780 (2009).
31. Minn, A. J. *et al.* Genes that mediate breast cancer metastasis to lung. *Nature* **436**, 518–524 (2005).
32. Cordenonsi, M. *et al.* The Hippo transducer TAZ confers cancer stem cell-related traits on breast cancer cells. *Cell* **147**, 759–772 (2011).
33. Dupont, S. *et al.* Role of YAP/TAZ in mechanotransduction. *Nature* **474**, 179–183 (2011).

34. Piccolo, S., Dupont, S. & Cordenonsi, M. The Biology of YAP/TAZ: Hippo Signaling and Beyond. *Physiol. Rev.* **94**, 1287–1312 (2014).
35. Totaro, A., Panciera, T. & Piccolo, S. YAP/TAZ upstream signals and downstream responses. *Nat. Cell Biol.* **20**, 888–899 (2018).
36. Aragona, M. *et al.* A Mechanical Checkpoint Controls Multicellular Growth through YAP/TAZ Regulation by Actin-Processing Factors. *Cell* **154**, 1047–1059 (2013).
37. Lamar, J. M. *et al.* The Hippo pathway target, YAP, promotes metastasis through its TEAD-interaction domain. *Proc. Natl. Acad. Sci.* **109**, E2441–E2450 (2012).
38. Moroishi, T., Hansen, C. G. & Guan, K.-L. The emerging roles of YAP and TAZ in cancer. *Nat. Rev. Cancer* **15**, 73–79 (2015).
39. Nallet-Staub, F. *et al.* Pro-Invasive Activity of the Hippo Pathway Effectors YAP and TAZ in Cutaneous Melanoma. *J. Invest. Dermatol.* **134**, 123–132 (2014).
40. Pan, D. The Hippo Signaling Pathway in Development and Cancer. *Dev. Cell* **19**, 491–505 (2010).
41. Sero, J. E. *et al.* Cell shape and the microenvironment regulate nuclear translocation of NF-κB in breast epithelial and tumor cells. *Mol. Syst. Biol.* **11**, 790 (2015).
42. Sero, J. E. & Bakal, C. Multiparametric Analysis of Cell Shape Demonstrates that β-PIX Directly Couples YAP Activation to Extracellular Matrix Adhesion. *Cell Syst.* **4**, 84-96.e6 (2017).
43. Zhao, B. *et al.* TEAD mediates YAP-dependent gene induction and growth control. *Genes Dev.* **22**, 1962–1971 (2008).
44. Harvey, K. F., Zhang, X. & Thomas, D. M. The Hippo pathway and human cancer. *Nat. Rev. Cancer* **13**, 246–257 (2013).
45. COSMIC database.
46. Calses, P. C., Crawford, J. J., Lill, J. R. & Dey, A. Hippo Pathway in Cancer: Aberrant Regulation and Therapeutic Opportunities. *Trends Cancer* **5**, 297–307 (2019).
47. Fisher, M. L., Grun, D., Adhikary, G., Xu, W. & Eckert, R. L. Inhibition of YAP function overcomes BRAF inhibitor resistance in melanoma cancer stem cells. *Oncotarget* **8**, 110257–110272 (2017).
48. Kapoor, A. *et al.* Yap1 Activation Enables Bypass of Oncogenic Kras Addiction in Pancreatic Cancer. *Cell* **158**, 185–197 (2014).
49. Kim, M. H. *et al.* Actin remodeling confers BRAF inhibitor resistance to melanoma cells through YAP/TAZ activation. *EMBO J.* **35**, 462–478 (2016).
50. Kitajima, S. *et al.* Overcoming Resistance to Dual Innate Immune and MEK Inhibition Downstream of KRAS. *Cancer Cell* **34**, 439-452.e6 (2018).
51. Lin, L. *et al.* The Hippo effector YAP promotes resistance to RAF- and MEK-targeted cancer therapies. *Nat. Genet.* **47**, 250–256 (2015).
52. Nguyen, C. & Yi, C. YAP/TAZ Signaling and Resistance to Cancer Therapy. *Trends Cancer* **5**, 283–296 (2019).
53. Shao, D. D. *et al.* KRAS and YAP1 Converge to Regulate EMT and Tumor Survival. *Cell* **158**, 171–184 (2014).
54. Feng, X. *et al.* A Platform of Synthetic Lethal Gene Interaction Networks Reveals that the GNAQ Uveal Melanoma Oncogene Controls the Hippo Pathway through FAK. *Cancer Cell* **35**, 457-472.e5 (2019).
55. Feng, X. *et al.* Hippo-Independent Activation of YAP by the GNAQ Uveal

Melanoma Oncogene through a Trio-Regulated Rho GTPase Signaling Circuitry. *Cancer Cell* **25**, 831–845 (2014).
56. Lai, D., Ho, K. C., Hao, Y. & Yang, X. Taxol resistance in breast cancer cells is mediated by the hippo pathway component TAZ and its downstream transcriptional targets Cyr61 and CTGF. *Cancer Res.* **71**, 2728–2738 (2011).
57. Lin, C.-H. *et al.* Microenvironment rigidity modulates responses to the HER2 receptor tyrosine kinase inhibitor lapatinib via YAP and TAZ transcription factors. *Mol. Biol. Cell* **26**, 3946–3953 (2015).
58. Lionarons, D. A. *et al.* RAC1P29S Induces a Mesenchymal Phenotypic Switch via Serum Response Factor to Promote Melanoma Development and Therapy Resistance. *Cancer Cell* **36**, 68-83.e9 (2019).
59. Zanconato, F., Cordenonsi, M. & Piccolo, S. YAP/TAZ at the roots of cancer. *Cancer Cell* **29**, 783–803 (2016).
60. Pascual-Vargas, P. *et al.* RNAi screens for Rho GTPase regulators of cell shape and YAP/TAZ localisation in triple negative breast cancer. *Sci. Data* **4**, 170018 (2017).
61. Zhao, B. *et al.* Inactivation of YAP oncoprotein by the Hippo pathway is involved in cell contact inhibition and tissue growth control. *Genes Dev.* **21**, 2747–2761 (2007).
62. Piccolo, S., Cordenonsi, M. & Dupont, S. Molecular Pathways: YAP and TAZ Take Center Stage in Organ Growth and Tumorigenesis. *Clin. Cancer Res.* **19**, 4925–4930 (2013).
63. Miller, A. L. & Bement, W. M. Regulation of cytokinesis by Rho GTPase flux. *Nat. Cell Biol.* **11**, 71–77 (2009).
64. Su, K.-C., Takaki, T. & Petronczki, M. Targeting of the RhoGEF Ect2 to the equatorial membrane controls cleavage furrow formation during cytokinesis. *Dev. Cell* **21**, 1104–1115 (2011).
65. Ferrandez, Y. *et al.* Allosteric inhibition of the guanine nucleotide exchange factor DOCK5 by a small molecule. *Sci. Rep.* **7**, 1–13 (2017).
66. Di Agostino, S. *et al.* YAP enhances the pro-proliferative transcriptional activity of mutant p53 proteins. *EMBO Rep.* **17**, 188–201 (2016).
67. Lin, C. *et al.* YAP is essential for mechanical force production and epithelial cell proliferation during lung branching morphogenesis. *eLife* **6**,.
68. Mizuno, T. *et al.* YAP induces malignant mesothelioma cell proliferation by upregulating transcription of cell cycle-promoting genes. *Oncogene* **31**, 5117–5122 (2012).
69. Rosenbluh, J. *et al.* β-Catenin-Driven Cancers Require a YAP1 Transcriptional Complex for Survival and Tumorigenesis. *Cell* **151**, 1457–1473 (2012).
70. Schlegelmilch, K. *et al.* Yap1 Acts Downstream of α-Catenin to Control Epidermal Proliferation. *Cell* **144**, 782–795 (2011).
71. Yu, F.-X. *et al.* Protein kinase A activates the Hippo pathway to modulate cell proliferation and differentiation. *Genes Dev.* **27**, 1223–1232 (2013).
72. Lehmann, B. D. *et al.* Identification of human triple-negative breast cancer subtypes and preclinical models for selection of targeted therapies. *J. Clin. Invest.* **121**, 2750–2767 (2011).
73. Kumar, S. S. *et al.* KRAS G13D Mutation and Sensitivity to Cetuximab or Panitumumab in a Colorectal Cancer Cell Line Model. *Gastrointest. Cancer Res. GCR* **7**, 23–26 (2014).
74. Tokumaru, Y. *et al.* KRAS signaling enriched triple negative breast

cancer is associated with favorable tumor immune microenvironment and better survival. *Am. J. Cancer Res.* **10**, 897–907 (2020).
75. Huang, J. *et al.* The implication from RAS/RAF/ERK signaling pathway increased activation in epirubicin treated triple negative breast cancer. *Oncotarget* **8**, 108249–108260 (2017).
76. van der Noord, V. E. *et al.* An increased cell cycle gene network determines MEK and Akt inhibitor double resistance in triple-negative breast cancer. *Sci. Rep.* **9**, (2019).
77. Bado, I. & Zhang, X. H.-F. Senesce to Survive: YAP-Mediated Dormancy Escapes EGFR/MEK Inhibition. *Cancer Cell* **37**, 1–2 (2020).
78. Coggins, G. E. *et al.* YAP1 mediates resistance to MEK1/2 inhibition in neuroblastomas with hyperactivated RAS signalling. *Cancer Res.* (2019) doi:10.1158/0008-5472.CAN-19-1415.
79. Bakal, C., Aach, J., Church, G. & Perrimon, N. Quantitative Morphological Signatures Define Local Signaling Networks Regulating Cell Morphology. *Science* **316**, 1753–1756 (2007).
80. Yin, Z. *et al.* A screen for morphological complexity identifies regulators of switch-like transitions between discrete cell shapes. *Nat. Cell Biol.* **15**, 860–871 (2013).
81. He, Y. *et al.* CdGAP is required for transforming growth factor β- and Neu/ErbB-2-induced breast cancer cell motility and invasion. *Oncogene* **30**, 1032–1045 (2011).
82. LaLonde, D. P., Grubinger, M., Lamarche-Vane, N. & Turner, C. E. CdGAP Associates with Actopaxin to Regulate Integrin-Dependent Changes in Cell Morphology and Motility. *Curr. Biol.* **16**, 1375–1385 (2006).
83. Wormer, D., Deakin, N. O. & Turner, C. E. CdGAP regulates cell migration and adhesion dynamics in two-and three-dimensional matrix environments. *Cytoskeleton* **69**, 644–658 (2012).
84. Jenna, S. *et al.* The Activity of the GTPase-activating Protein CdGAP Is Regulated by the Endocytic Protein Intersectin. *J. Biol. Chem.* **277**, 6366–6373 (2002).
85. Lamarche-Vane, N. & Hall, A. CdGAP, a Novel Proline-rich GTPase-activating Protein for Cdc42 and Rac. *J. Biol. Chem.* **273**, 29172–29177 (1998).
86. McCormack, J. J. *et al.* The scaffold protein Ajuba suppresses CdGAP activity in epithelia to maintain stable cell-cell contacts. *Sci. Rep.* **7**, 1–14 (2017).
87. Nguyen, T. T. T. *et al.* PLEKHG3 enhances polarized cell migration by activating actin filaments at the cell front. *Proc. Natl. Acad. Sci.* **113**, 10091–10096 (2016).
88. Festa, B. P. *et al.* OCRL deficiency impairs endolysosomal function in a humanized mouse model for Lowe syndrome and Dent disease. *Hum. Mol. Genet.* **28**, 1931–1946 (2019).
89. Williams, C., Choudhury, R., McKenzie, E. & Lowe, M. Targeting of the type II inositol polyphosphate 5-phosphatase INPP5B to the early secretory pathway. *J. Cell Sci.* **120**, 3941–3951 (2007).
90. Cau, J. Cdc42 controls the polarity of the actin and microtubule cytoskeletons through two distinct signal transduction pathways. *J. Cell Sci.* **118**, 2579–2587 (2005).
91. Hall, A. Small GTP-Binding Proteins and the Regulation of the Actin Cytoskeleton. *Annu. Rev. Cell Biol.* **10**, 31–54 (1994).

92. Johnson, D. I. & Pringle, J. R. Molecular characterization of CDC42, a Saccharomyces cerevisiae gene involved in the development of cell polarity. *J. Cell Biol.* **111**, 143–152 (1990).
93. Stowers, L., Yelon, D., Berg, L. J. & Chant, J. Regulation of the polarization of T cells toward antigen-presenting cells by Ras-related GTPase CDC42. *Proc. Natl. Acad. Sci.* **92**, 5027–5031 (1995).
94. Sapudom, J. *et al.* The phenotype of cancer cell invasion controlled by fibril diameter and pore size of 3D collagen networks. *Biomaterials* **52**, 367–375 (2015).
95. Gadea, G. & Blangy, A. Dock-family exchange factors in cell migration and disease. *Eur. J. Cell Biol.* **93**, 466–477 (2014).
96. Zanconato, F. *et al.* Genome-wide association between YAP/TAZ/TEAD and AP-1 at enhancers drives oncogenic growth. *Nat. Cell Biol.* **17**, 1218–1227 (2015).
97. Etienne-Manneville, S. & Hall, A. Cdc42 regulates GSK-3b and adenomatous polyposis coli to control cell polarity. **421**, 4 (2003).
98. Brognard, J., Sierecki, E., Gao, T. & Newton, A. C. PHLPP and a Second Isoform, PHLPP2, Differentially Attenuate the Amplitude of Akt Signaling by Regulating Distinct Akt Isoforms. *Mol. Cell* **25**, 917–931 (2007).
99. Xiong, X., Li, X., Wen, Y.-A. & Gao, T. Pleckstrin Homology (PH) Domain Leucine-rich Repeat Protein Phosphatase Controls Cell Polarity by Negatively Regulating the Activity of Atypical Protein Kinase C. *J. Biol. Chem.* **291**, 25167–25178 (2016).
100. Brunet, A. *et al.* Protein Kinase SGK Mediates Survival Signals by Phosphorylating the Forkhead Transcription Factor FKHRL1 (FOXO3a). *Mol. Cell. Biol.* **21**, 952–965 (2001).
101. Manning, B. D. & Toker, A. AKT/PKB Signaling: Navigating the Network. *Cell* **169**, 381–405 (2017).
102. O'Brien, W. T. *et al.* Glycogen synthase kinase-3 is essential for β-arrestin-2 complex formation and lithium-sensitive behaviors in mice. *J. Clin. Invest.* **121**, 3756–3762 (2011).
103. Erdal, E., Ozturk, N., Cagatay, T., Eksioglu-Demiralp, E. & Ozturk, M. Lithium-mediated downregulation of PKB/Akt and cyclin E with growth inhibition in hepatocellular carcinoma cells. *Int. J. Cancer* **115**, 903–910 (2005).
104. Huang, J., Guo, X., Li, W. & Zhang, H. Activation of Wnt/β-catenin signalling via GSK3 inhibitors direct differentiation of human adipose stem cells into functional hepatocytes. *Sci. Rep.* **7**, 1–12 (2017).
105. Schleicher, S. B. *et al.* Combined application of arsenic trioxide and lithium chloride augments viability reduction and apoptosis induction in human rhabdomyosarcoma cell lines. (2017).
106. Wu, D. & Pan, W. GSK3: a multifaceted kinase in Wnt signaling. *Trends Biochem. Sci.* **35**, 161–168 (2010).
107. Etienne-Manneville, S. & Hall, A. Integrin-Mediated Activation of Cdc42 Controls Cell Polarity in Migrating Astrocytes through PKCζ. *Cell* **106**, 489–498 (2001).
108. Clevers, H. & Nusse, R. Wnt/β-Catenin Signaling and Disease. *Cell* **149**, 1192–1205 (2012).
109. Ciani, L., Krylova, O., Smalley, M. J., Dale, T. C. & Salinas, P. C. A divergent canonical WNT-signaling pathway regulates microtubule dynamics. *J. Cell Biol.* **164**, 243–253 (2004).

110. Zhang, S. *et al.* The Tumor Suppressor LKB1 Regulates Lung Cancer Cell Polarity by Mediating cdc42 Recruitment and Activity. *Cancer Res.* **68**, 740–748 (2008).
111. Frank, S. R. *et al.* The focal adhesion-associated proteins DOCK5 and GIT2 comprise a rheostat in control of epithelial invasion. *Oncogene* **36**, 1816–1828 (2017).
112. Cohen, J. *Statistical power analysis for the behavioral sciences*. (Psychology Press, 1988).
113. Sawilowsky, S. S. New Effect Size Rules of Thumb. *J. Mod. Appl. Stat. Methods* **8**, 597–599 (2009).
114. Pasapera, A. M. *et al.* Rac1-Dependent Phosphorylation and Focal Adhesion Recruitment of Myosin IIA Regulates Migration and Mechanosensing. *Curr. Biol.* **25**, 175–186 (2015).
115. Guimbal, S. *et al.* Dock5 is a new regulator of microtubule dynamic instability in osteoclasts. *Biol. Cell* boc.201900014 (2019) doi:10.1111/boc.201900014.
116. Ogawa, K. *et al.* DOCK5 functions as a key signaling adaptor that links FcεRI signals to microtubule dynamics during mast cell degranulation. *J. Exp. Med.* **211**, 1407–1419 (2014).
117. Waterman-Storer, C. M., Worthylake, R. A., Liu, B. P., Burridge, K. & Salmon, E. D. Microtubule growth activates Rac1 to promote lamellipodial protrusion in fibroblasts. *Nat. Cell Biol.* **1**, 45–50 (1999).
118. Wittmann, T., Bokoch, G. M. & Waterman-Storer, C. M. Regulation of leading edge microtubule and actin dynamics downstream of Rac1. *J. Cell Biol.* **161**, 845–851 (2003).
119. Chiou, J.-G., Balasubramanian, M. K. & Lew, D. J. Cell Polarity in Yeast. *Annu. Rev. Cell Dev. Biol.* **33**, 77–101 (2017).
120. Johnson, J. M., Jin, M. & Lew, D. J. Symmetry breaking and the establishment of cell polarity in budding yeast. *Curr. Opin. Genet. Dev.* **21**, 740–746 (2011).
121. Richman, T. J., Sawyer, M. M. & Johnson, D. I. Saccharomyces cerevisiae Cdc42p localizes to cellular membranes and clusters at sites of polarized growth. *Eukaryot. Cell* **1**, 458–468 (2002).
122. Kozubowski, L. *et al.* Symmetry-breaking polarization driven by a Cdc42p GEF-PAK complex. *Curr. Biol. CB* **18**, 1719–1726 (2008).
123. Howell, A. S. *et al.* Negative feedback enhances robustness in the yeast polarity establishment circuit. *Cell* **149**, 322–333 (2012).
124. Wu, C.-F. *et al.* Role of competition between polarity sites in establishing a unique front. *eLife* **4**, e11611 (2015).
125. Freisinger, T. *et al.* Establishment of a robust single axis of cell polarity by coupling multiple positive feedback loops. *Nat. Commun.* **4**, 1807 (2013).
126. Case, L. B. & Waterman, C. M. Integration of actin dynamics and cell adhesion by a three-dimensional, mechanosensitive molecular clutch. *Nat. Cell Biol.* **17**, 955–963 (2015).
127. Nobes, C. D. & Hall, A. Rho, Rac, and Cdc42 GTPases regulate the assembly of multimolecular focal complexes associated with actin stress fibers, lamellipodia, and filopodia. *Cell* **81**, 53–62 (1995).
128. Ando, K. *et al.* Rap1 potentiates endothelial cell junctions by spatially controlling myosin II activity and actin organization. *J. Cell Biol.* **202**, 901–916 (2013).

129. Kim, N.-G. & Gumbiner, B. M. Adhesion to fibronectin regulates Hippo signaling via the FAK–Src–PI3K pathway. *J. Cell Biol.* **210**, 503–515 (2015).
130. Calvo, F. *et al.* Mechanotransduction and YAP-dependent matrix remodelling is required for the generation and maintenance of cancer-associated fibroblasts. *Nat. Cell Biol.* **15**, 637–646 (2013).
131. Dongre, A. & Weinberg, R. A. New insights into the mechanisms of epithelial–mesenchymal transition and implications for cancer. *Nat. Rev. Mol. Cell Biol.* **20**, 69–84 (2019).
132. Brown, E. *et al.* Dynamic imaging of collagen and its modulation in tumors in vivo using second-harmonic generation. *Nat. Med.* **9**, 796–800 (2003).
133. Magzoub, M., Jin, S. & Verkman, A. S. Enhanced macromolecule diffusion deep in tumors after enzymatic digestion of extracellular matrix collagen and its associated proteoglycan decorin. *FASEB J.* **22**, 276–284 (2008).
134. Oldberg, A. *et al.* Collagen-binding proteoglycan fibromodulin can determine stroma matrix structure and fluid balance in experimental carcinoma. *Proc. Natl. Acad. Sci.* **104**, 13966–13971 (2007).
135. Sabeh, F. *et al.* Tumor cell traffic through the extracellular matrix is controlled by the membrane-anchored collagenase MT1-MMP. *J. Cell Biol.* **167**, 769–781 (2004).
136. Sabeh, F., Shimizu-Hirota, R. & Weiss, S. J. Protease-dependent versus -independent cancer cell invasion programs: three-dimensional amoeboid movement revisited. *J. Cell Biol.* **185**, 11–19 (2009).
137. Stamov, D. R. & Pompe, T. Structure and function of ECM-inspired composite collagen type I scaffolds. *Soft Matter* **8**, 10200 (2012).
138. Wolf, K. *et al.* Compensation mechanism in tumor cell migration: mesenchymal–amoeboid transition after blocking of pericellular proteolysis. *J. Cell Biol.* 11 (2003).
139. Sapudom, J. *et al.* Fibril bending stiffness of 3D collagen matrices instructs spreading and clustering of invasive and non-invasive breast cancer cells. *Biomaterials* **193**, 47–57 (2019).
140. Vinci, M., Box, C. & Eccles, S. A. Three-Dimensional (3D) Tumor Spheroid Invasion Assay. *J. Vis. Exp.* (2015) doi:10.3791/52686.
141. Tyanova, S. *et al.* The Perseus computational platform for comprehensive analysis of (prote)omics data. *Nat. Methods* **13**, 731–740 (2016).
142. Ho, J., Tumkaya, T., Aryal, S., Choi, H. & Claridge-Chang, A. Moving beyond P values: data analysis with estimation graphics. *Nat. Methods* **16**, 565–566 (2019).
143. Kluyver, T. *et al.* Jupyter Notebooks—a publishing format for reproducible computational workflows. 4.
144. https://software.broadinstitute.org/morpheus.
145. Berginski, M. E., Vitriol, E. A., Hahn, K. M. & Gomez, S. M. High-Resolution Quantification of Focal Adhesion Spatiotemporal Dynamics in Living Cells. *PLOS ONE* **6**, e22025 (2011).

Figure 1 DOCK5 regulates YAP/TAZ localisation.

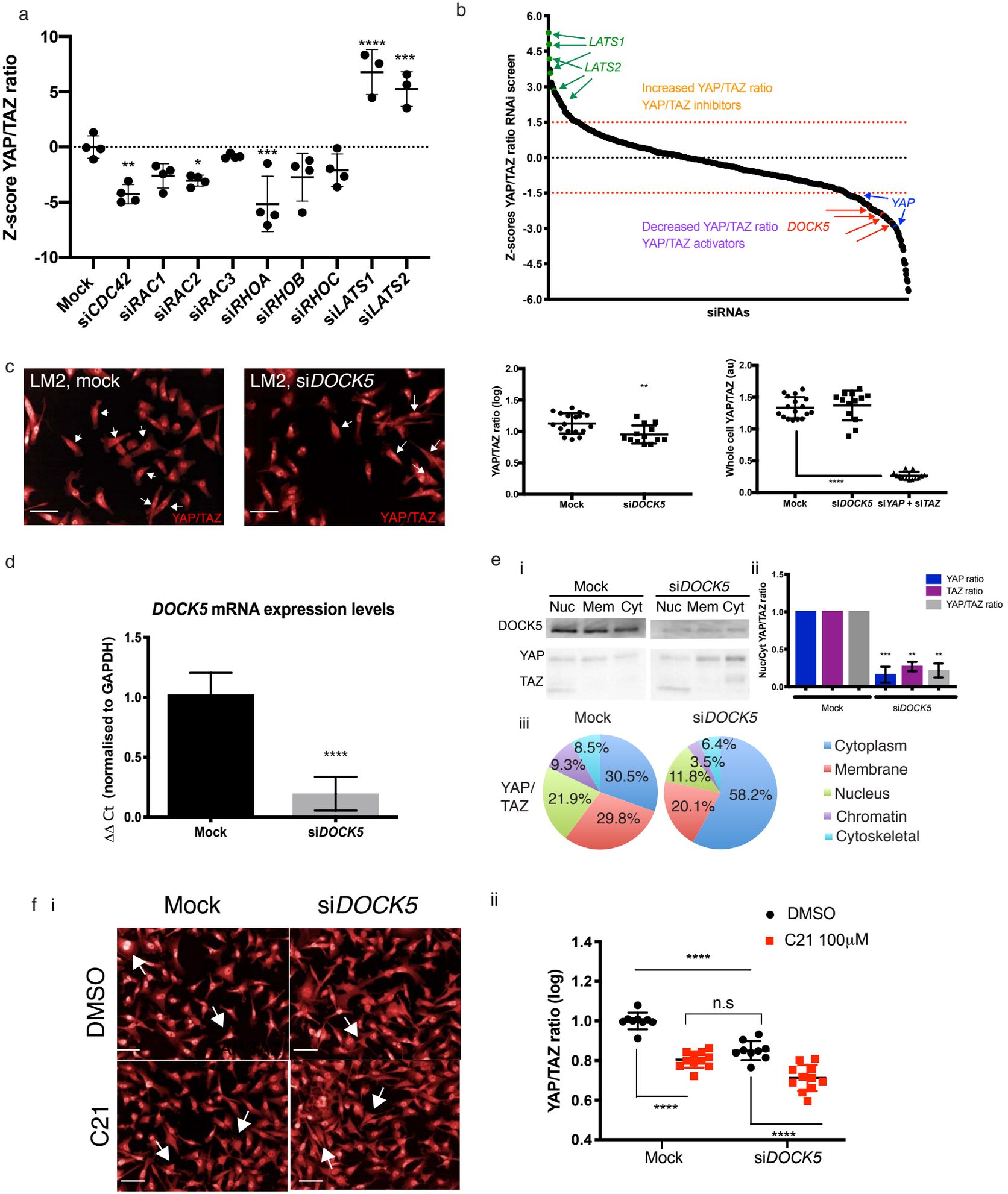

Figure 2 DOCK5 contributes to growth and drug resistance in LM2 cells

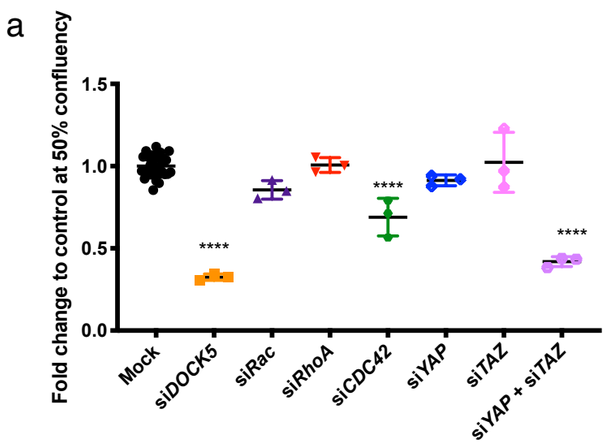

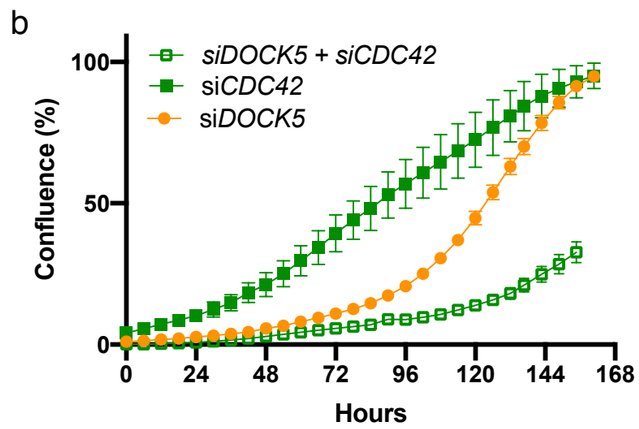

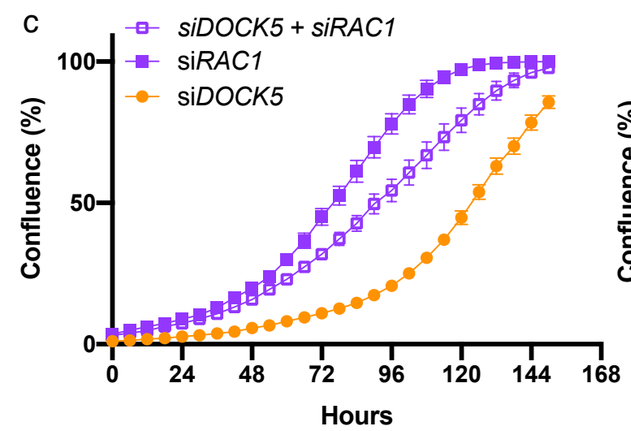

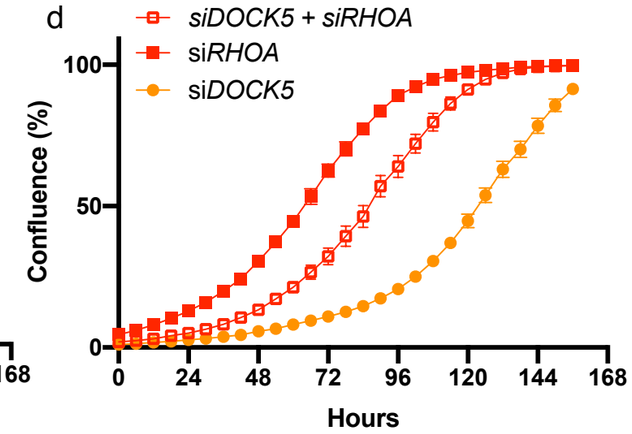

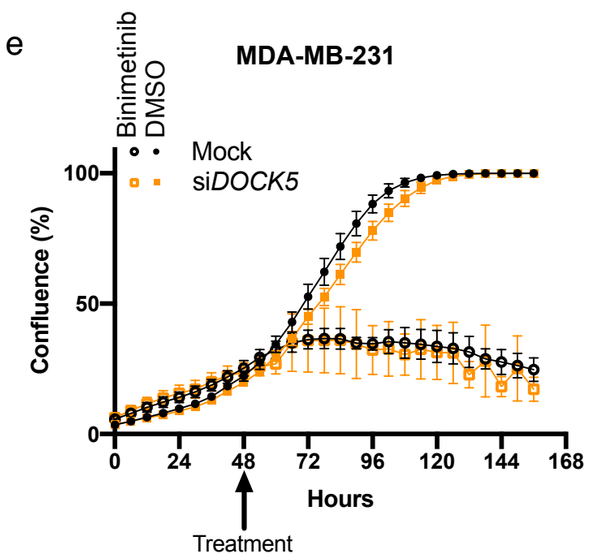

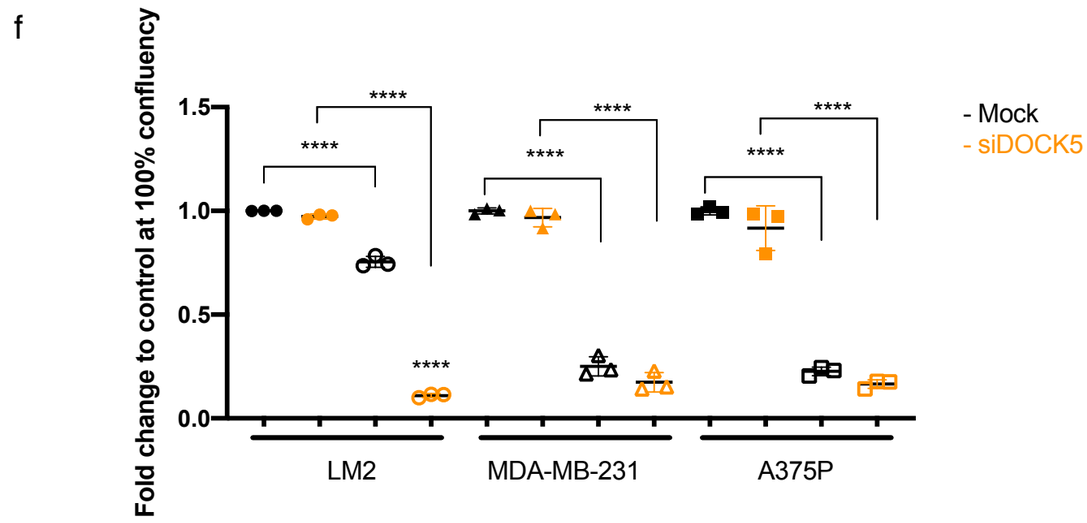

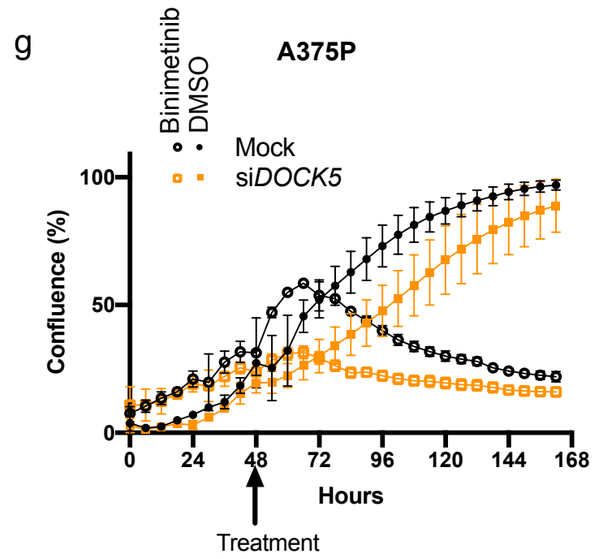

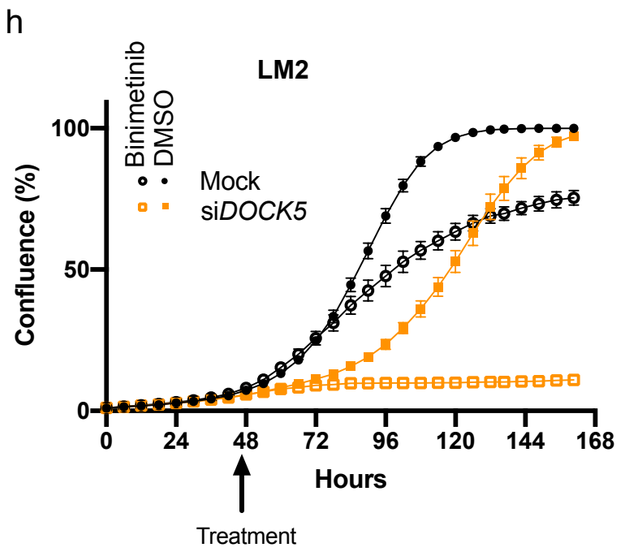

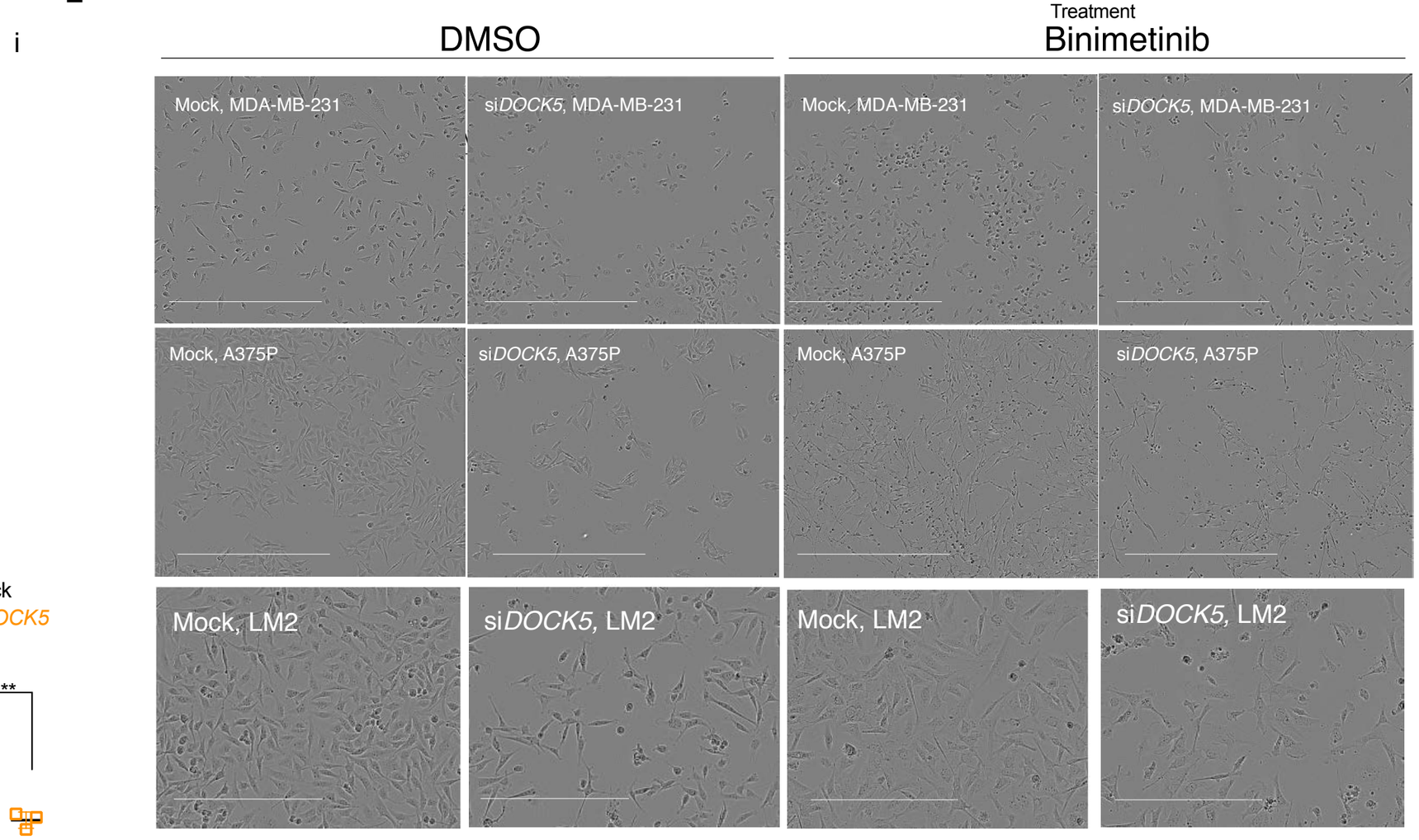

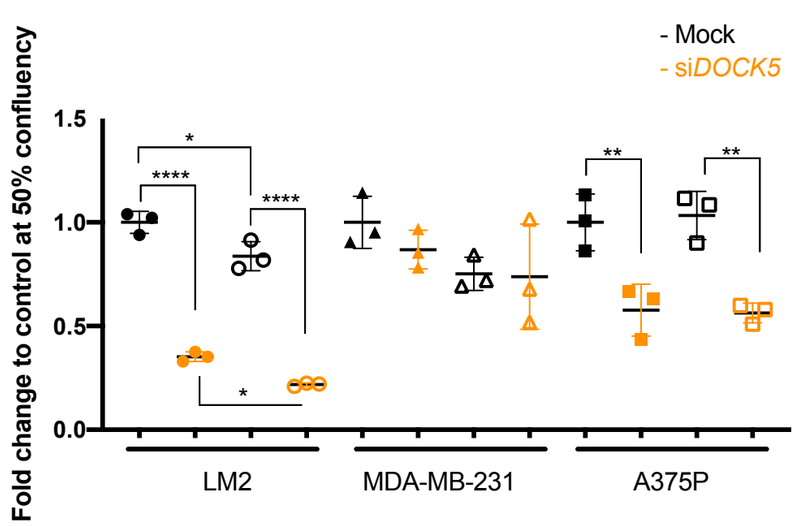

Figure 3 Shape classification and relationship with YAP/TAZ

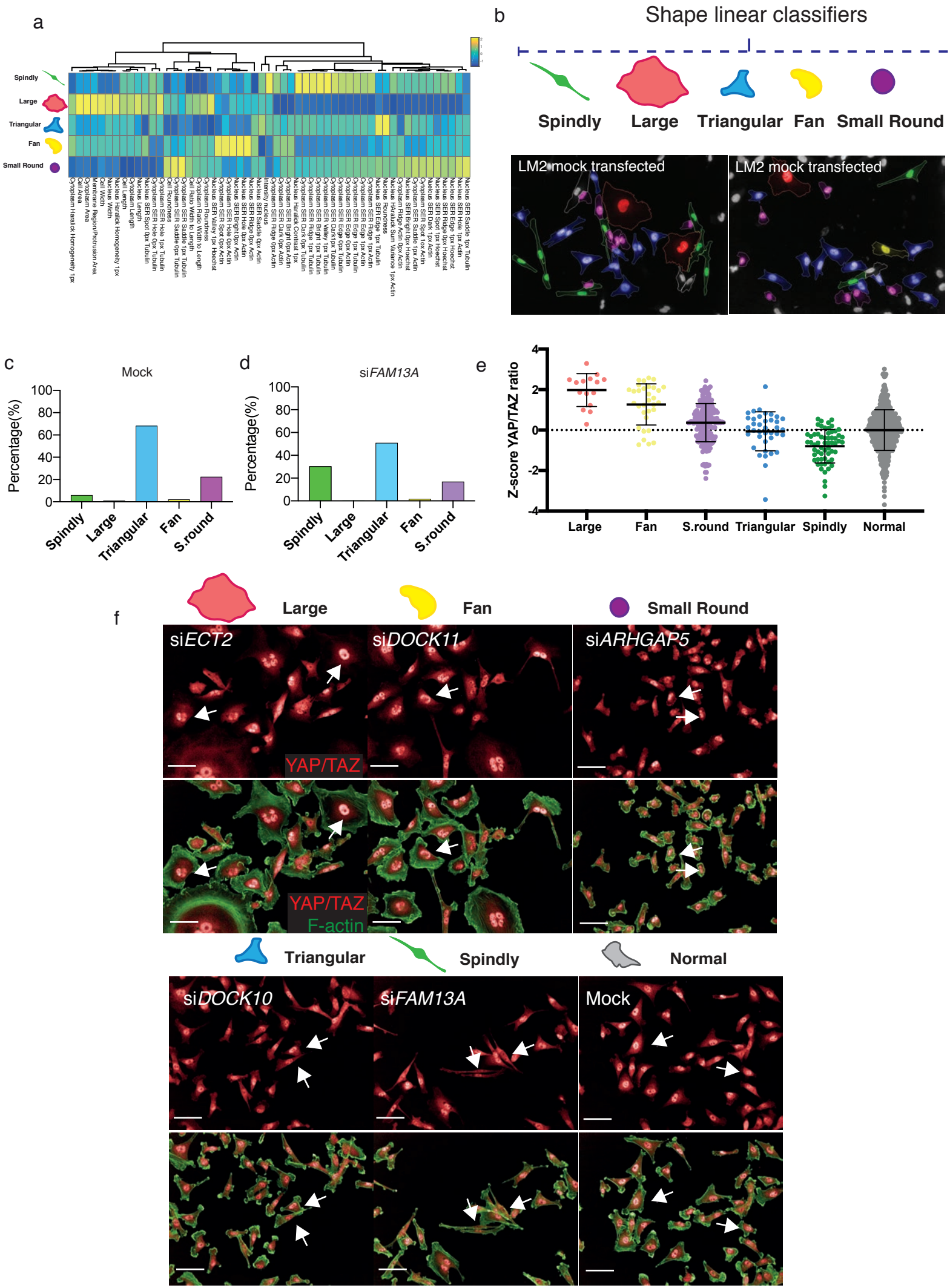

Figure 4 DOCK5 regulates shape

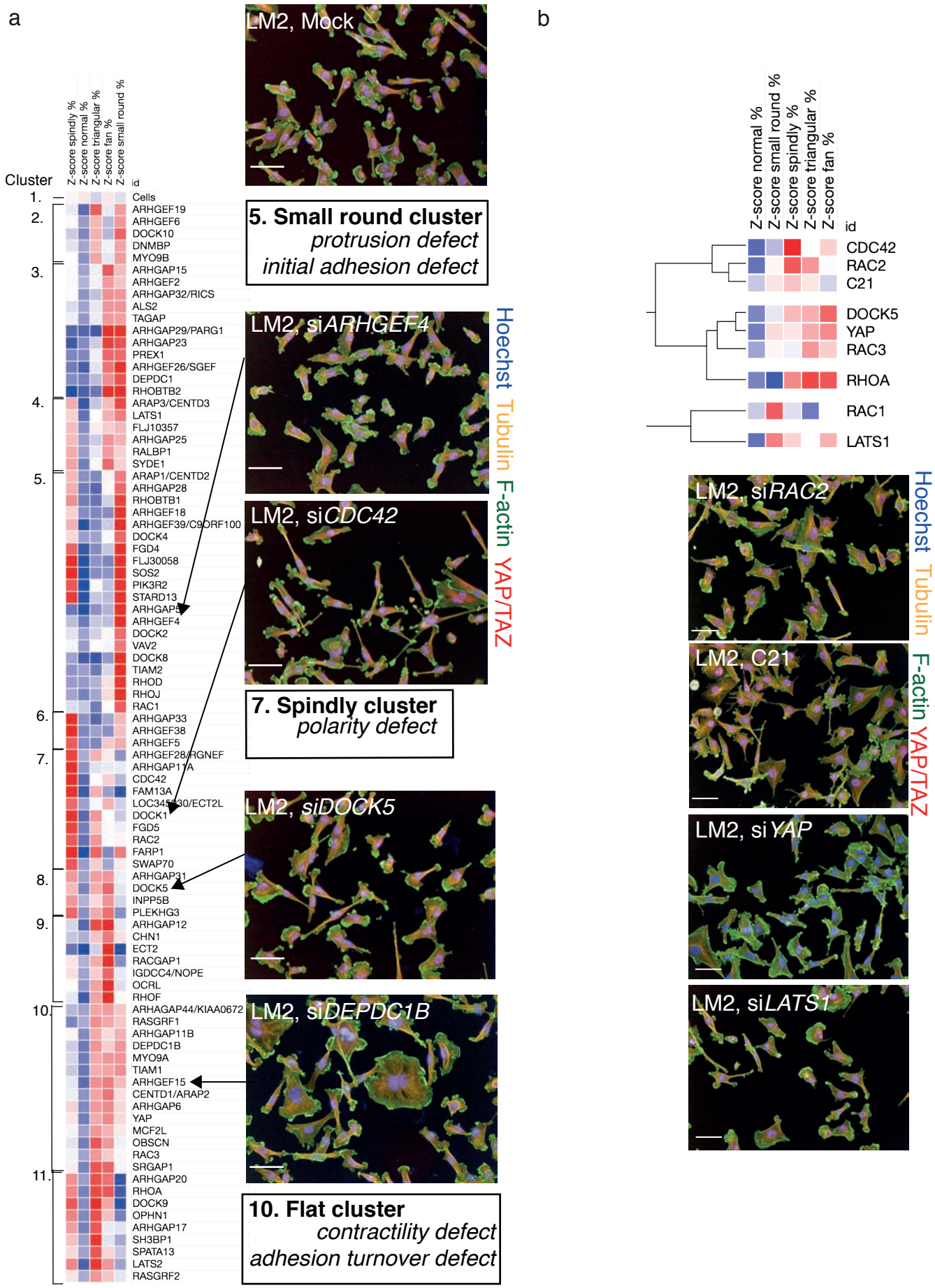

Figure 5 DOCK5 depletion reduces single cell invasion in 3D collagen assays and Matrigel spheroid assays

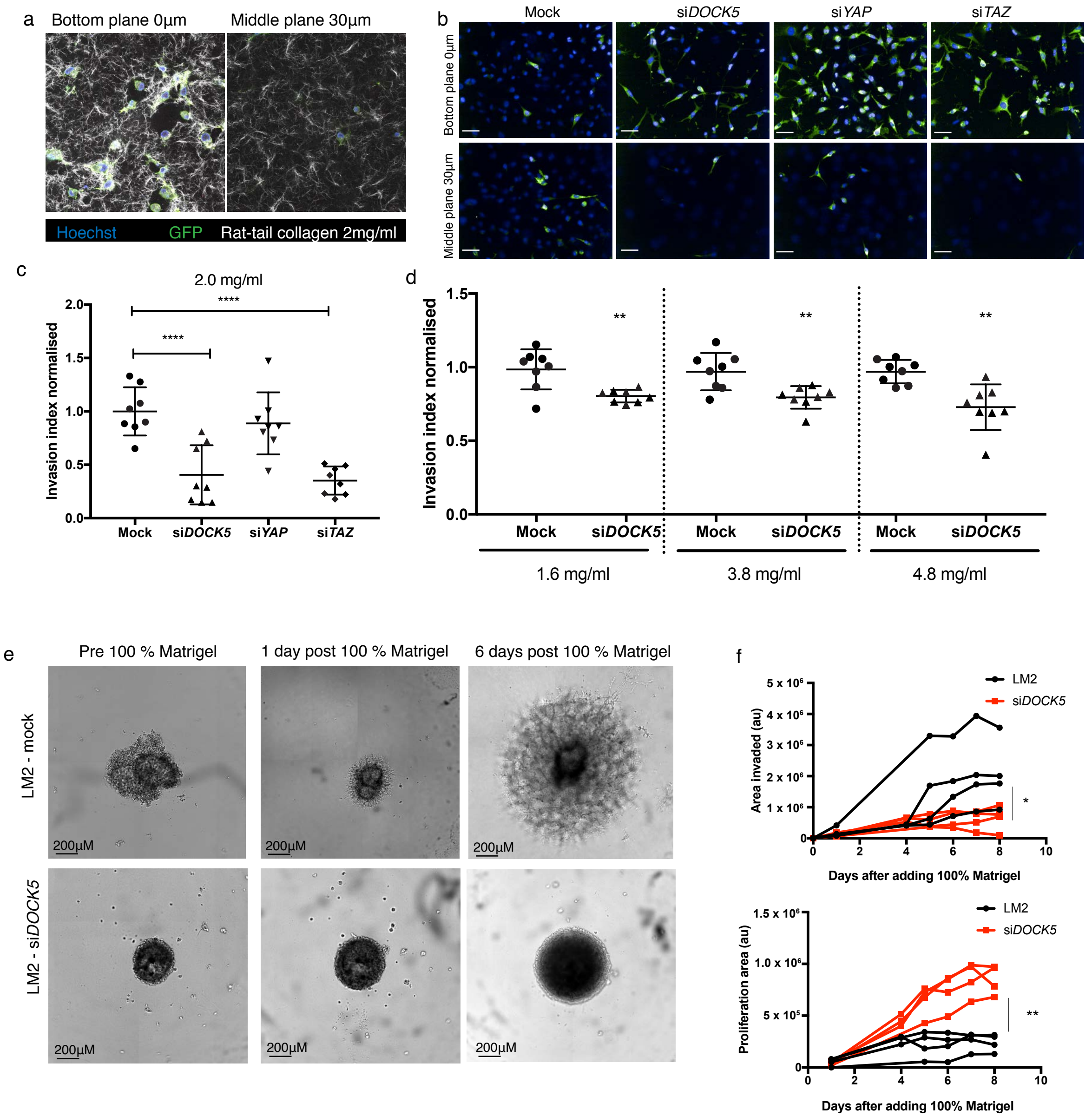

Figure 6 DOCK5 depletion alters protein levels of regulators of polarity

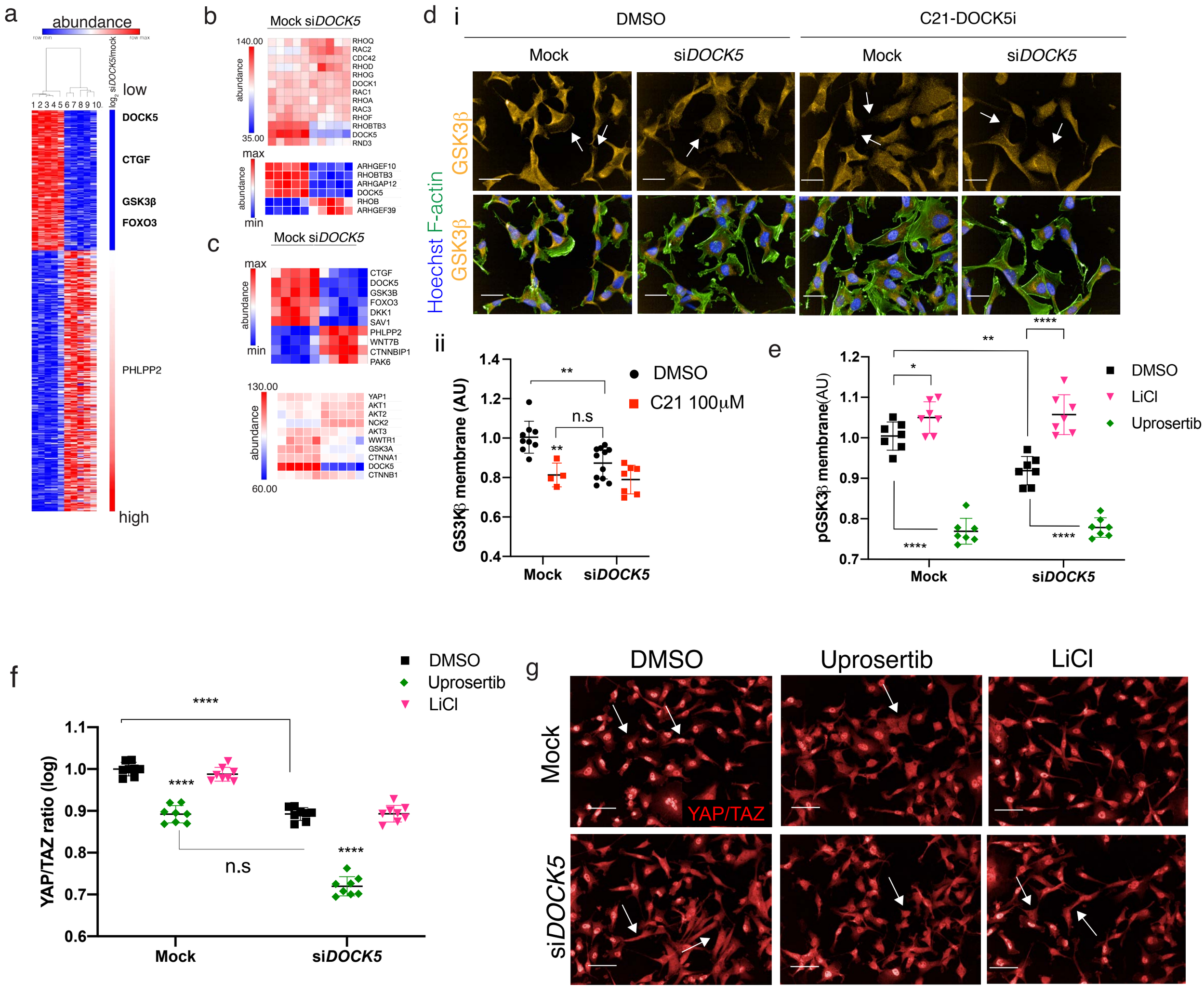

Figure 7 DOCK5 depletion reduces wound closure rates and affects Golgi orientation

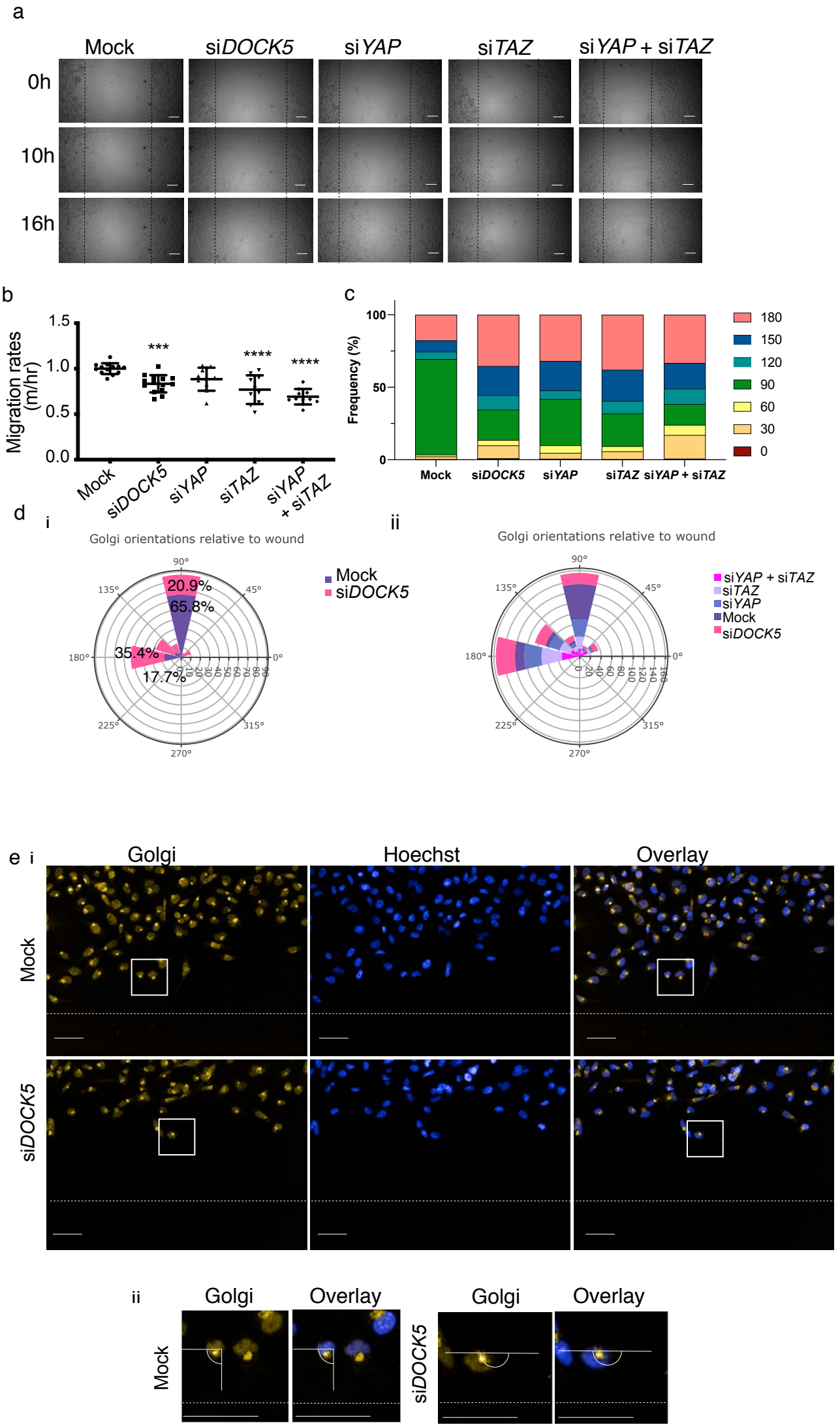

Figure 8 DOCK5 depletion alters focal adhesion dynamics

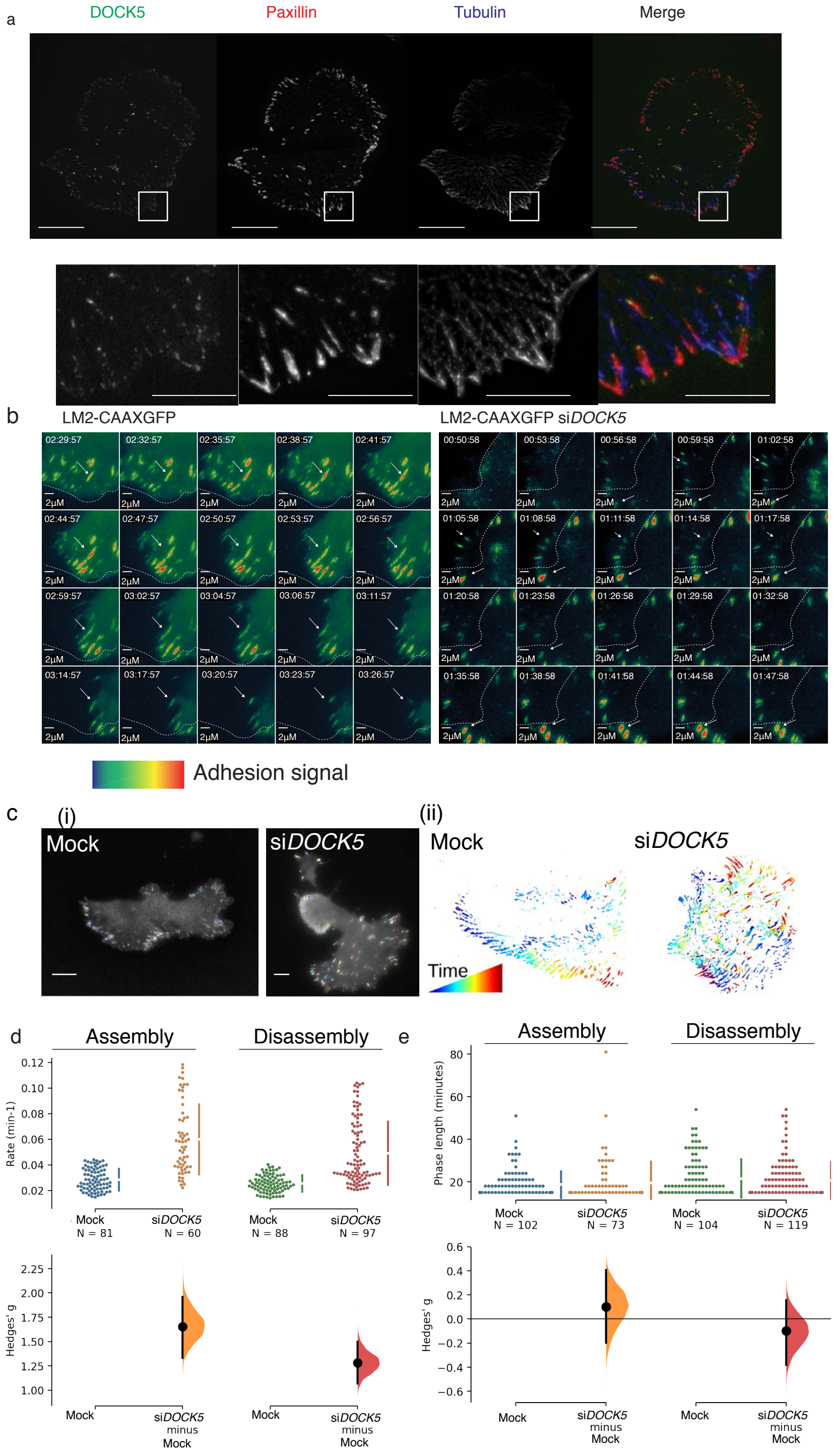

Figure 9 CDC42 and RHOA depletion affect FA morphogenesis in metastatic cells

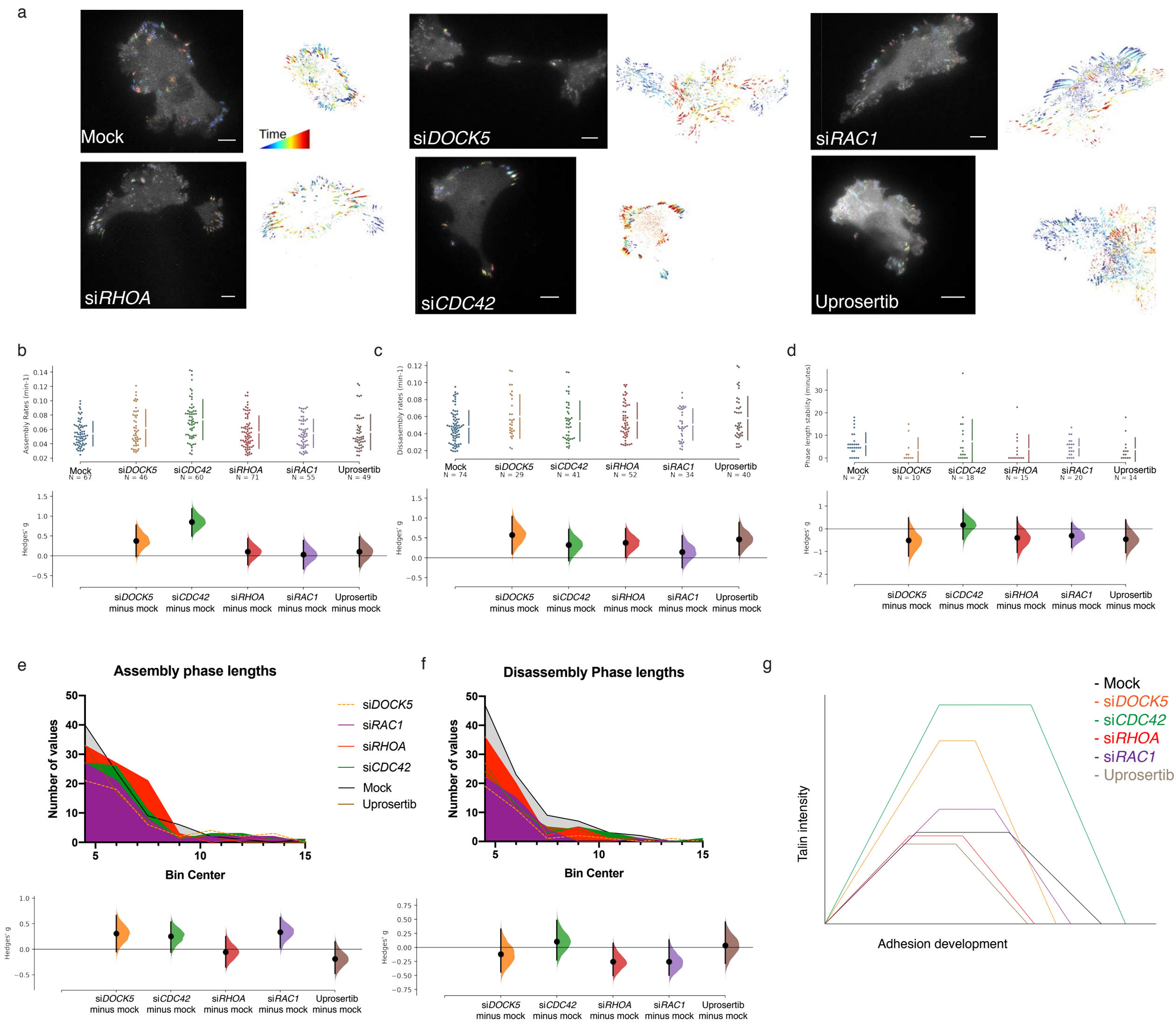

Figure 10 DOCK5 and CDC42 promote polarity

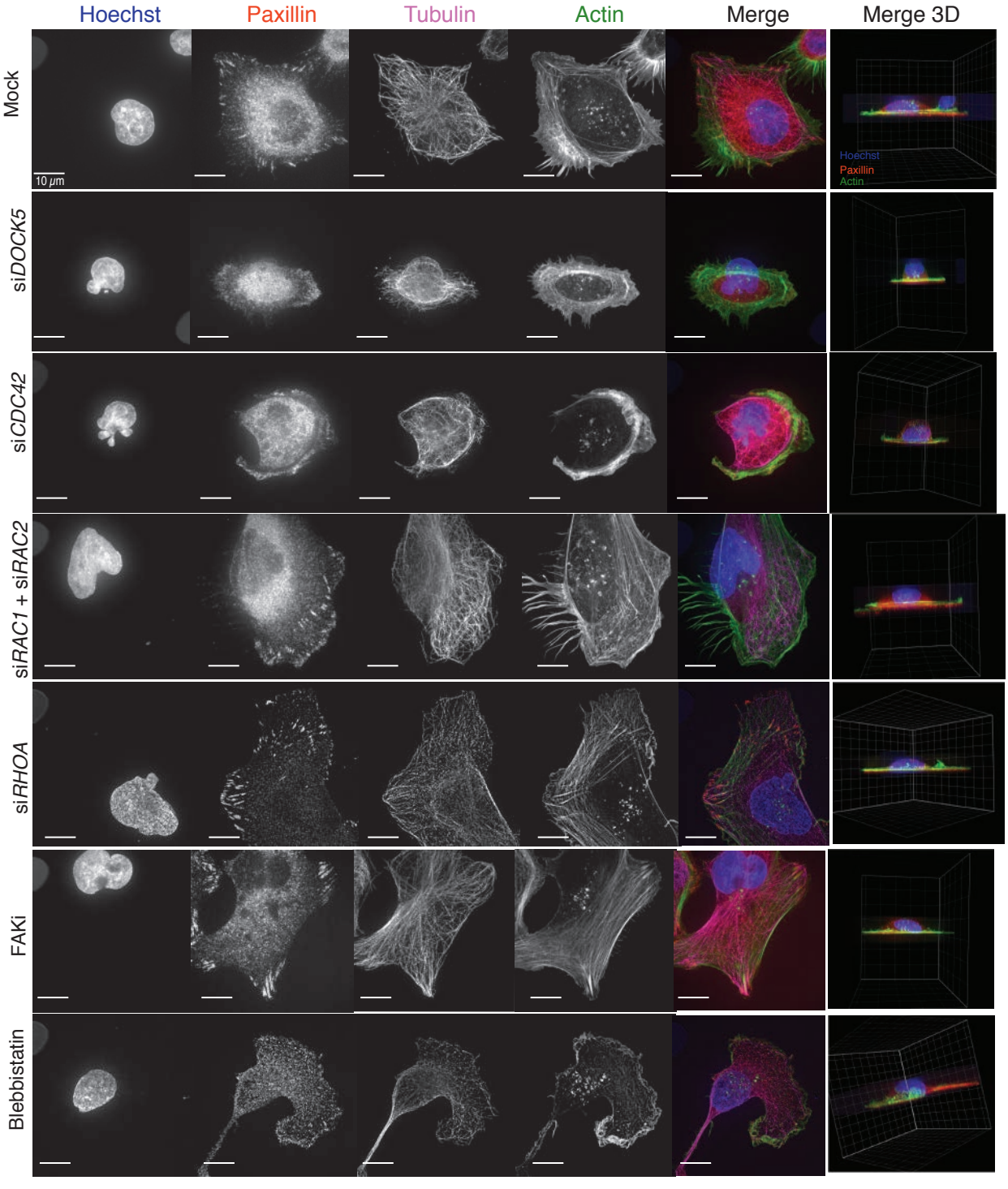

Figure 11 DOCK5 promotes spreading following MT depolymerisation

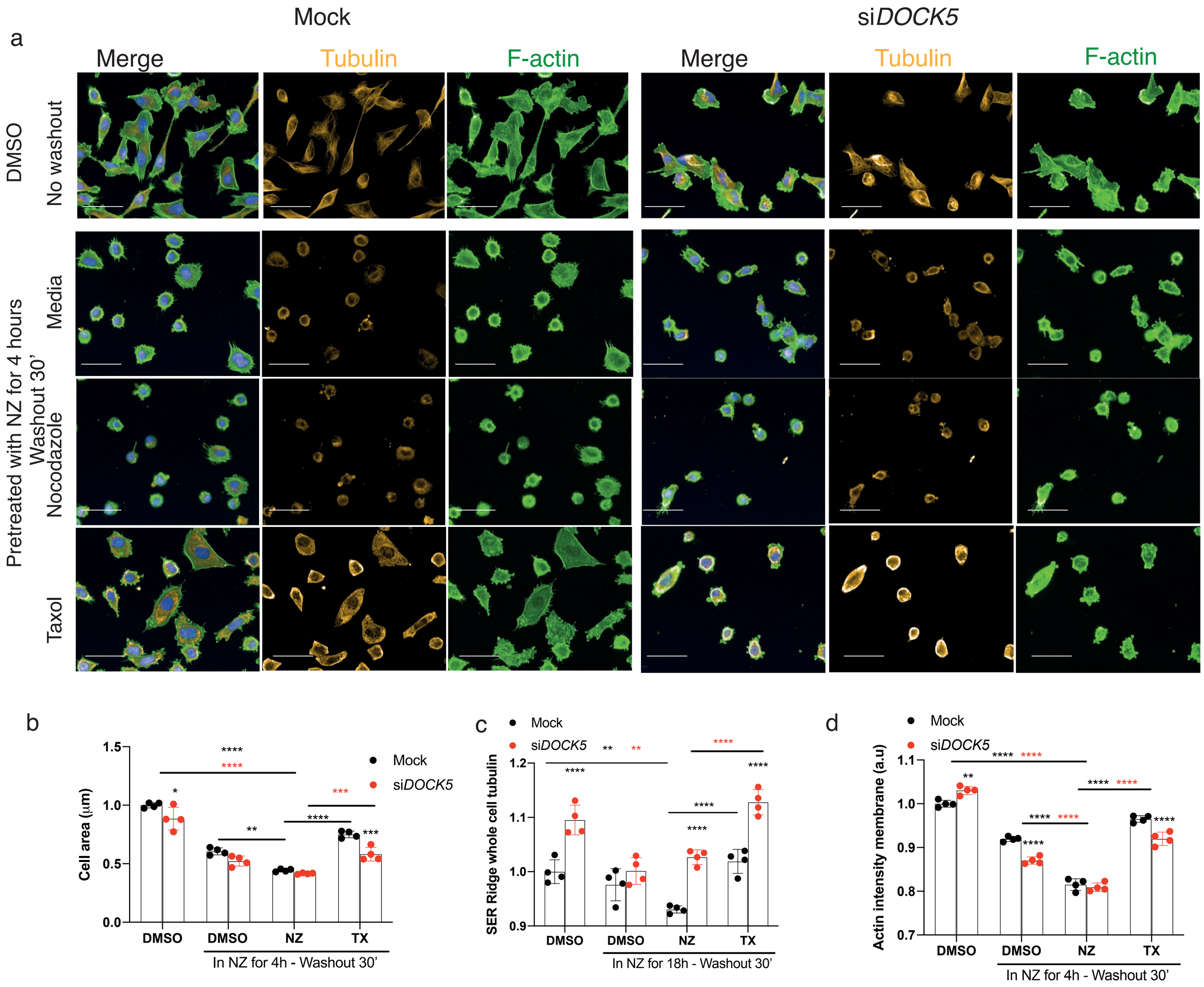
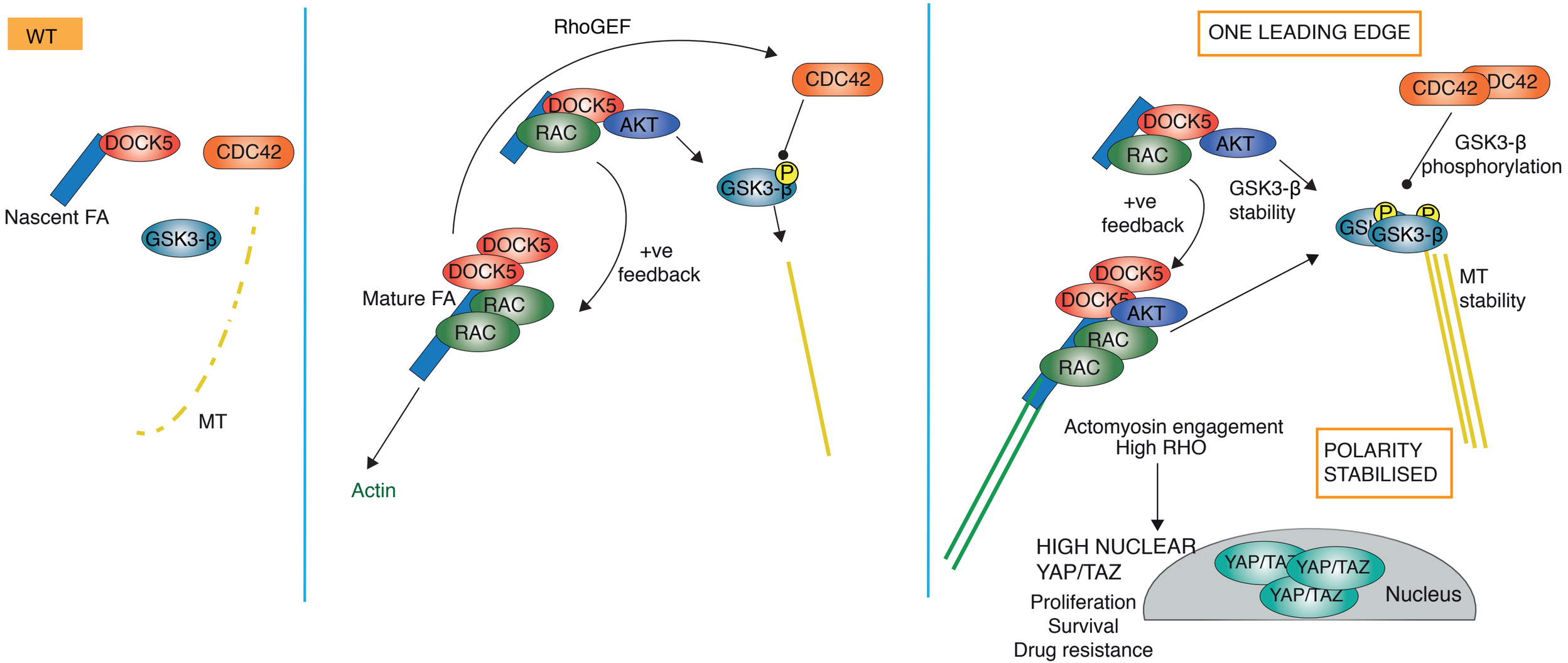
Figure 12 DOCK5 acts at FAs in breast cells to establish positive feedback loops which maintain polarity